Supporting Information: Chemically accurate simulation of a polyatomic molecule-metal surface reaction

Francesco Nattino[†], *Davide Migliorini*[†], *Geert-Jan Kroes*, [*,†], *Eric Dombrowski*[‡], *Eric A. High*[‡], *Daniel R. Killelea*[||], *Arthur L. Utz*[*,‡]

[†]Leiden Institute of Chemistry, Leiden University, Gorlaeus Laboratories, P.O. Box 9502, 2300 RA Leiden, The Netherlands

[‡]Department of Chemistry and W. M. Keck Foundation Laboratory for Materials Chemistry Tufts University, Medford, MA 02155, United States

[||]Department of Chemistry & Biochemistry, Loyola University Chicago, 1068 W Sheridan Rd., Chicago, IL 60660, United States

1. Experimental Methods.

1.1 General approach.

All experiments were performed in a supersonic molecular beam-surface scattering chamber located at Tufts University [1-8]. Specific details on the design and characterization of our apparatus and on our experimental methods can be found in Refs. [4-8]. Dilute (1-2%) mixtures of CHD_3 in H_2 expanded continuously from a temperature-controlled molecular beam nozzle source maintained at temperature T_n. Varying T_n from 550 to 900 K produced beams with experimentally measured and well-defined incident translational energy distributions (E_i) ranging from 101 to 160 kJ/mol with $\Delta E_i / E_i \approx 5\%$. The CHD_3 molecules impinged on a clean 550K Ni(111) surface along the surface normal. We generally selected beam conditions where the total energy of the incident CHD_3 molecules exceeded the threshold energy for reaction by 15 kJ/mol or more. Under these conditions, we expect reactivity to be dominated by classical, "over the barrier" trajectories where the quasi-classical trajectory (QCT) method is most applicable. Two sets of experiments were performed.

We first measured S_0 for a supersonic molecular beam of CHD_3 molecules incident on a clean Ni(111) surface at selected values of E_i. Translational and rotational degrees of freedom cooled efficiently during supersonic expansion, but vibrational cooling was not complete. Therefore, these experiments, which did not involve any laser excitation, yielded reaction probabilities averaged over the vibrational state distribution in the molecular beam. We refer to these values of S_0 as S_0^{off} (the laser-off reaction probability). We used values of S_0^{off} for the two beams with E_i = 112 and 121 kJ/mol to constrain the mixing parameter x in the specific reaction parameter (SRP) functional defined by Eq. 1 of the manuscript.

In the second set of experiments, we measured the rovibrational state resolved value of S_0 for CHD_3 molecules prepared in a single vibrationally excited quantum state. In these state-resolved experiments, not only was the reagent molecules' E_i controlled, but their vibrational energy (E_{vib}), vibrational motion (mode), and rotational energy (E_{rot}) were also precisely defined. The state-selected molecules were prepared in their vibrationally excited state with infrared absorption. A narrow bandwidth infrared laser ($\Delta\nu$ < 1MHz) delivered 1W of light to excite a fraction, f_{exc}, of CHD_3 molecules in the beam from v"=0, J"=1, K"=0 to v'=1, J'=2, K'=0 of the ν_1 C-H stretching vibration via the R(1) (ΔK=0) transition at 3005.538 cm^{-1}. To obtain S_0 for molecules in the laser excited state, $S_0^{v_1=1}$, we first measured the average S_0 for all molecules in the laser-excited molecular beam, which we denote as S_0^{on} (the laser-on reaction probability). We calculated the state-resolved reaction probability, $S_0^{v_1=1}$, using our measured values of S_0^{on}, S_0^{off}, and f_{exc} along with an estimate of the vibrational ground state reactivity, $S_0^{v=0}$. Further details of our experimental methods, results, and data analysis follow.

1.2 Molecular Beam and Surface Preparation

In all experiments, a supersonic molecular beam formed when 25 psig of the CHD_3 / H_2 gas mixture expanded continuously through a 35-μm diameter orifice in an Inconel 600 nozzle source. A type-K thermocouple spot welded to the nozzle source face and located 1 mm from the orifice provided a measure of T_n. A temperature controller maintained T_n within ± 1K of the desired value. Gas mixture compositions ranged from 1-2% of CHD_3 (Cambridge Isotope Laboratories, isotopic purity = 98%) diluted in H_2 (99.9999%, Airgas). After expanding through the nozzle source orifice, the beam was skimmed and triply differentially pumped before

impinging on a clean Ni(111) single crystal. A dry ice/acetone trap and a gas polisher (Supelco Supel-Pure-O) removed trace reactive impurities, including CO, H_2O, O_2, and unsaturated hydrocarbons, from the CHD_3 /H_2 gas mix before it entered the nozzle source. To verify that reactive impurities were not impacting our reactivity measurements, we exposed a clean Ni(111) surface held at 550 K to a beam expanding from a room temperature nozzle source. Under these conditions, ($E_i \approx 60$ kJ/mol) over 97% of all CHD_3 molecules were in the vibrational ground state, and S_0 for CHD_3 was well below our molecular beam reflectivity detection limit. We verified that for dose durations used in these studies, no detectable surface contaminants accumulated on the surface.

The Ni(111) crystal (Surface Preparation Laboratory) was cut and polished within 0.1° of the (111) plane, as verified by monochromatic X-ray diffraction. This miscut angle corresponds to an average single-atom step density of about 0.5%. The crystal was housed in an ultrahigh vacuum (UHV) chamber whose base pressure was 1.0×10^{-10} Torr. Heating the surface to 1000 K for 30 seconds, sputtering with 500eV Ar^+ ions for 15 minutes, and then annealing at 1000K for 45 minutes produced a clean surface with impurity levels below the ≈ 0.01 ML (monolayer) detection limit of our Auger electron spectrometer.

1.3 Molecular Beam Characterization

The extent of translational, rotational, and vibrational cooling in the molecular beam impacts both calculations and experiment. For a realistic comparison with the experiments, calculated reaction probabilities need to be averaged over the measured translational energy distribution in the beam, and calculations of S_0^{off} must take into account the distribution of vibrational states in the beam. The extent of vibrational and rotational cooling also defines the fractional population

of laser-excited CHD_3 molecules, f_{exc}, that can be prepared in state resolved experiments. The R(1) ($\Delta K=0$) infrared excitation transition at 3005.538 cm^{-1} only accesses molecules in the v"=0, J"=1, K"=0 initial state. If vibrational cooling is incomplete, fewer than 100% of the molecules are in v"=0. Similarly, the extent of rotational cooling determines the fraction of v"=0 molecules in the J"=1, K"=0 rotational rotational level of v"=0. The following sub-sections describe our characterization of the beam's translational energy and the distribution of vibrational and rotational states in the beam.

1.3.1 Translational Energy Distribution

We performed neutral time-of-flight measurements on all beams used in this study. A mechanical chopper wheel rotating at 300Hz modulated the molecular beam. A quadrupole mass spectrometer (UTI 100C) located on the molecular beam axis measured the arrival time distribution of the chopped beam, and a multichannel scaler recorded the data. Fitting the arrival time data to a density-weighted Gaussian distribution function [9] yielded a stream velocity, v_0, and width parameter, α, that characterized the velocity distribution of CHD_3 molecules in the beam. The flux weighted velocity distribution is [9-10]

$$f(v) = N_v v^3 \exp\left(-\left[\left(v - v_0\right)/\alpha\right]^2\right) \qquad \text{(S1)}$$

where N_v is a normalization constant. The fitting procedure we used properly accounted for electronic and ion-flight time delays, deconvoluted the known gating function of the chopper wheel assembly from the arrival time distribution, and yielded the inherent velocity distribution of CHD_3 molecules in the beam [11]. Table S1 lists T_n, v_0, and α for all beams used in these experiments. The Ab Initio Molecular Dynamics (AIMD) calculations used these speed

distributions to ensure that simulations of the experimental data properly accounted for the spread of E_i present in the incident beam.

Electronic delays and ion flight times in the quadrupole mass spectrometer can lead to errors in the time of flight analysis if not properly accounted for [12]. We used the following procedure to determine electronic and ion flight time delays and to characterize the translational energy distribution of the beams.

We first inserted a fixed length extender on our molecular beam apparatus to extend the neutral molecular beam flight path. We then measured arrival time distributions with and without the extender and calculated the difference in arrival time for the two QMS positions. We performed these measurements for pure He, H_2 and CH_4 beams as well as dilute (1-2%) seeded beams of CHD_3 and CH_4 in H_2, each at at a series of nozzle source temperatures ranging from 300 to 1000K. Since electronic and ion flight time delays are identical with or without the extender in place, dividing the known length of the extender by the shift in arrival time for the beam at the two QMS locations provided a measure of beam speed that was independent of electronic or ion flight time delays in the system. We refer to this method of obtaining the beam's speed as the extender method.

We then used the measure of the beam's average stream velocity from the extender method to quantify the fixed electronic delay in our time of flight measurements as well as the mass-dependent ion flight times. For each unique beam/nozzle source temperature combination, we constrained the stream velocity, v_0, to the value obtained in the extender method, and adjusted the sum of electronic and ion flight time delays, along with N_v and α, in a non-linear least squares fit of the arrival time distributions obtained with and without the extender [11]. Since the ion energy of the mass spectrometer was fixed at a value 10 or more times greater than the

incident kinetic energy of any beam studied, the ion flight time should scale with the reciprocal square root of the ion mass/charge (m/z) ratio. We collected the delays associated with each of the beams and plotted them vs. $\sqrt{1/m}$ where m was the mass of the singly charged ion detected in the time of flight measurement. The data for all of the gases and gas mixes at the full range of nozzle temperatures fell, as expected, on a straight line. The y-axis intercept gave a measure of the mass-independent electronic delay, which is the time delay between the digital start pulse that defines t=0 for the multichannel scaler and the time when the chopper wheel gating slot is centered on the molecular beam axis. The slope of the line, multiplied by $\sqrt{1/m}$, allowed us to predict the ion flight time for all of the singly charged ions detected in our time of flight measurements [12]. Finally, we used these measured values of electronic delay and ion flight time to fit the arrival time distribution of each beam at a fixed QMS location to obtain the stream velocity, v_o, and width parameter, α. We refer to this method as the single path length method.

We confirmed that the single path length and the extender methods for determining E_i yielded speed distributions for pure He and H_2 beams that differed by less than 1% in stream velocity for values of T_n ranging from 300 to 1000K. Furthermore, stream velocity values for the He beams were within 1% of those predicted using the known heat capacity of He. The v_o and α values reported in Table S1 were obtained from analysis of arrival time distributions using the single path length method, and were validated by measurements with the path length extender.

1.3.2 Vibrational State Distribution

While extensive rotational cooling of CHD_3 occurred during supersonic expansion, the extent of vibrational cooling was much more limited, and significant populations of thermally excited vibrational states were present in the beam at elevated T_n.

In order to model S_0 for the laser off studies, AIMD calculations must properly account for the presence of vibrationally excited states in the beam. A full spectroscopic characterization of the beam is the most general way of quantifying these state populations. Bronnikov et al. [13] used this approach to quantify the extent of vibrational cooling in supersonic expansions of pure methane (CH_4). They used infrared absorption spectroscopy of the beam and compared the intensity of hot band transitions that originated in thermally excited vibrational states to the intensity of transitions originating in the vibrational ground state [13]. A full knowledge of the oscillator strengths of these transitions allowed them to translate peak intensities into populations. We have performed a limited set of analogous measurements in our lab for pure CH_4 beams, and we find that the vibrational cooling we observe in our apparatus follows the pattern of intrapolyad cooling reported in Ref. [13]. Unfortunately the very dilute gas mixtures used in this study (1-2% CHD_3 in H_2) resulted in much lower signal levels than we were able to obtain for pure CH_4 beams. As a result we were unable to measure directly the excited state vibrational populations for CHD_3 in these experiments. Instead, we built on our understanding of vibrational cooling dynamics in the beam and prior studies of vibrational cooling in the CH_4 isotopologue to address this point.

We first verified that our measurement of T_n was accurate. We used the measured T_n and the known heat capacity of He to predict the arrival time distribution of pure He beams. The excellent agreement between the experimentally measured and predicted values of E_i validated our measurement of T_n.

We next considered how T_n and collisional energy transfer during supersonic expansion affected vibrational state populations in the beam. Vibrational energy transfer processes that transfer significant quantities of vibrational energy ($\Delta E > kT$) into translational degrees of

freedom (and therefore "cool" the vibrational state distribution) are generally much less efficient than those that thermalize rotational or translational degrees of freedom [14]. As a result, the limited number of collisions that occur during supersonic expansion are often insufficient to convert the energy of excited vibrational states into translational energy, and the beam retains a significant portion of its vibrational heat capacity in the form of thermally excited vibrational states in the beam.

Bronnikov et al. [13] found that the excited vibrational state populations for supersonic molecular beams of CH_4 reflected this behavior. Clusters of nearly degenerate vibrational states (polyads) showed significant *intra*polyad vibrational cooling since the energy gap between states within the polyad was less than kT. On the other hand, essentially no vibrational cooling occurred between states separated by 3kT or more. Therefore, the integrated population of each polyad was set by the nozzle temperature T_n and did not change appreciably upon expansion. Intrapolyad cooling among the nearly degenerate vibrations of each polyad did occur and shifted population from the highest E_{vib} members of the polyad to the lowest energy vibrational states within the polyad. A Boltzmann distribution at T_n accurately predicted the relative population of the polyads, while a temperature of about 1/5 of T_n predicted the relative population of vibrational states within a polyad. Therefore, the overall vibrational state population in the beam resembled a thermal Boltzmann distribution, but within each polyad intrapolyad cooling skewed population toward the lowest energy states. In Fig. S1, we apply the intrapolyad cooling model [13] to a T_n = 700K beam of CHD_3 with $T_{polyad} \approx T_n / 5$, and we compare the predicted vibrational state populations of the model with a Boltzmann distribution of vibrational states at the same T_n.

AIMD calculations of S_0^{off}, described in Section 2.5, yield reaction probabilities averaged over a Boltzmann population of vibrational states in the beam. We tested the sensitivity of these

calculations to intrapolyad vibrational cooling by reweighting the vibrational state populations to values consistent with the intrapolyad cooling reported by Bronnikov et al. [13]. While the modified vibrational state populations do alter the relative contribution of each vibrational state to S_0^{off}, including effects of intrapolyad cooling has negligible effects on the predicted values of S_0^{off} for the laser off molecular beams, which we summarize in Table S2.

Vibrational state populations affect the fraction of v=0 molecules available for excitation to the ν_1 C-H stretching state, and therefore f_{exc}. Since the v=0 level is separated from the next higher vibrational state by a large energy gap, we expect negligible collisional vibrational relaxation from thermally excited states into v=0 during supersonic expansion. Therefore, intrapolyad cooling does not alter the population of v=0 and both models of vibrational population predict the same fractional populations for the initial vibrational state (v"=0) of our infrared excitation transition.

1.3.3 Rotational State Distribution

Our extremely dilute CHD_3 in H_2 gas mixes prevented us from having sufficient dynamic range in our infrared absorption measurements to spectroscopically characterize the extent of rotational cooling in CHD_3 at high T_n. In prior work, we have measured the extent of rotational cooling for dilute mixes of CH_4 in H_2 [12] and CH_4 in He [15] in our apparatus. We recorded infrared absorption spectra of all v=0 rotational levels with $J \leq 5$ at nozzle source temperatures ranging from 300 to 500K, and we obtained rotational temperatures, T_{rot}, for each beam. We then related the observed rotational temperature to T_n and found that $T_{rot} \approx 0.0247\ T_n$ [15]. Assuming analogous rotational cooling dynamics for CHD_3 led to the estimated fractional rotational state populations f_{rot} listed in Table S3 for the J"=1, K"=0 rotational level of CHD_3.

1.4 Infrared Laser Excitation of CHD_3 in the Molecular Beam

State-resolved measurements of S_0 quantified the reactivity of beams in which a laser excited a fraction of the beam into the desired excited vibrational state. In those "laser on" experiments, one watt of infrared light from a single mode continuous wave infrared laser (Aculight Argos) crossed the molecular beam in a collision free region of the supersonic expansion. A parallel multipass mirror assembly was aligned slightly out of parallel to create a series of laser-molecular beam crossings, each orthogonal to a slightly different Doppler subset of molecules in the gently diverging molecular beam [7]. Spatially resolved Auger Electron Spectroscopy verified that the reactive flux of laser excited molecules impinging on the Ni(111) surface was uniform across the entire molecular beam.

The laser was tuned to excite CHD_3 from v"=0, J"=1, K"=0 to v'=1, J'=2, K'=0 of the ν_1 C-H stretching vibration via the R(1) (ΔK=0) transition at 3005.538 cm^{-1}. Since the narrow bandwidth laser excited a single rovibrational eigenstate, time-dependent intramolecular vibrational redistribution (IVR) did not occur in the gas phase molecule [16]. Since the radiative lifetime of C-H stretching states is much longer than the ca. 200 μs flight time from excitation region to the surface [17], the state-selected molecules approached the surface in their initially prepared vibrational state.

We used a room temperature pyroelectric bolometer (Eltec model 406-0) translated into the molecular beam path to quantify infrared absorption by CHD_3 in the molecular beam [18]. The bolometer detector responds to *changes* in the energy flux reaching the detector. During an absorption experiment, the molecular beam nozzle source is held at a constant temperature, and the molecular beam is not modulated. Therefore, the energy flux due to the beam's translational and internal energy is constant, and the bolometer signal does not respond to this constant energy

flux. To detect absorption, we use an electromechanical shutter to apply a square wave modulation to the infrared laser. When the laser is off resonance, the bolometer signal is zero because molecules in the beam do not absorb infrared light, and the energy flux remains constant, even though the laser is being modulated. As the laser is tuned into resonance and begins to excite CHD_3, the energy flux to the bolometer increases and then decreases as the laser is blocked and unblocked by the modulating shutter. The bolometer detects this changing energy flux, and we detect absorption. The bolometer signal is maximum when the laser frequency is centered on the absorption profile of CHD_3 molecules in the beam.

The response of the room temperature bolometer is described by [19]

$$S = \eta \Phi A f_{exc} h\nu f_{accom} \qquad \text{(S2)}.$$

In Eq. S2, η is the detector responsivity at a modulation frequency of 0.4 Hz, (1.0 x 10^4 V / W), Φ is the flux of CHD_3 (on the order of 6 x 10^{14} molecules $cm^{-2}sec^{-1}$, but dependent on beam energy and nozzle temperature), A is the area of the 2.0 mm diameter detector element (0.031 cm^2), f_{exc} is the fraction of all CHD_3 molecules in the beam that are excited by the laser (see Table S3), $h\nu$ is the photon energy of the IR excitation (6.0 x 10^{-20} J for 3000 cm^{-1}), and f_{accom} is the average fractional accommodation of the absorbed photon energy that is dissipated in the pyroelectric detector element. For a cryogenically cooled bolometer where the gas condenses on the surface, f_{accom} is typically 1, but for a room temperature device, the fraction is less than one. In this study, η, A and hν are constant for all measurements. In prior experiments we measured the incident flux and f_{exc} for 100% CH_4 and seeded CH_4 / H_2 beams [12] over a wide range of molecular speeds. Based on those measurements we found that f_{accom} for the laser excited vibrational quantum on the rough, polycrystalline lithium tantalate detector surface was low

(about 3%), approximately constant as E_i ranged from 10 to 140 kJ/mol. Therefore, the pyroelectric bolometer signal is directly proportional to the product of the CHD_3 flux, Φ, and f_{exc}.

We use a computer controlled servo loop to lock the laser frequency to the transmission fringe of a 0.500 m temperature stabilized and vacuum jacketed Fabry-Perot étalon. Once the laser is tuned into resonance with the CHD_3 absorption feature, the servo system maintains that resonance condition for many hours. We then allow the laser to excite the beam continuously without modulation and we remove the pyroelectric detector from the beam path to perform surface reactivity measurements.

1.5 The measurement of S_0^{on} and the determination of $S_0^{v_1=1}$

Molecular beam reflectivity methods related to the King and Wells technique [20] were used to measure the initial reaction probability of CHD_3, averaged over all vibrational states in the beam, with and without laser excitation (S_0^{on} and S_0^{off}, respectively). Laser excitation transfers a fraction of the v=0 molecules in the beam to the desired vibrationally excited state. Since laser excitation does not alter the population of any other vibrational states, the calculated difference between S_0^{on} and S_0^{off} depends only on the change in v=0 and laser excited state populations and the state-resolved reaction probabilities for those two states. We have shown that the state-resolved $S_0^{v_1=1}$ is related to the difference of these sticking probabilities in the following way [1]

$$S_0^{v_1=1} = \frac{S_0^{on} - S_0^{off}}{f_{exc}} + S_0^{v=0} \qquad \text{(S3)}.$$

Calculating $S_0^{\nu_1=1}$ requires two additional quantities – the fraction of all CHD_3 molecules in the beam excited by the laser, f_{exc}, and S_0 for the v=0 vibrational ground state. The methods used to determine S_0^{on}, S_0^{off}, f_{exc}, and $S_0^{\nu=0}$ are discussed in this section.

1.5.1 Measuring S_0^{off}

Measurements of S_0^{off} were used to define our semi-empirical density functional, and will be used here to calculate $S_0^{\nu_1=1}$, for CHD_3 molecules in the v=1 C-H stretching state. To measure S_0^{off} we placed a moveable, inert gold-covered slide in front of the clean Ni(111) surface. A mass spectrometer tuned to m/z=15 monitored the partial pressure of CHD_3 in the chamber, first with the molecular beam blocked from entering the UHV chamber, and then with it entering the UHV chamber and scattering from the gold-covered slide. (We monitored m/z = 15 for two reasons. First, it is not a daughter ion of any background gases in our UHV chamber, so its background count rate is very low. Second, the m/z = 15 peak intensity is 4.5% that of the parent m/z = 19. This allows us to operate our mass spectrometer in a linear response regime (count rates less than 3MHz) while monitoring the partial pressure of CHD_3 during a molecular beam dose [15].) Next, we quickly retracted the slide from the beam path and allowed the beam to impinge on the clean Ni(111) surface. An initial drop in CHD_3 partial pressure results from a fraction of the beam reacting on the surface rather than scattering non-reactively into the gas phase. The ratio of the partial pressure drop due to reaction divided by the partial pressure rise when the beam enters the chamber provides a quantitative measure of S_0 [20]. We have verified that our implementation of this method to measure S_0 for CH_4 and CHD_3 agrees, within our reported error limits, with

previously published measurements that used other detection methods to quantify reactivity [1-3]. Figure S2 shows typical data for one of our sticking measurements.

1.5.2 Measuring S_0^{on}

To determine $S_0^{\nu_1=1}$, we must also measure S_0^{on} (Eq.S3). To do so, we tuned the laser into resonance with the desired infrared absorption transition, and used the computer controlled servo system described in Section 1.4 to maintain resonance with the absorption feature. We then used the molecular beam reflectivity method outlined for S_0^{off} measurements to quantify the average reactivity of molecules in the laser-excited beam, S_0^{on}.

1.5.3 Obtaining f_{exc}

Calculation of the state-resolved reaction probability, $S_0^{\nu_1=1}$, depends sensitively on f_{exc}, the fraction of all CHD_3 molecules in the molecular beam that are laser excited to the ν_1 state. In turn, f_{exc} depends on the fraction of all CHD_3 molecules in the beam that are in the correct initial state for the IR absorption transition (v"=0, J"=1, K"=0) times the fraction of those molecules that are excited by infrared absorption, f_{sat},

$$f_{exc} = f_{rot} f_{v=0} f_{sat} \qquad \text{(S4)}.$$

Reference [6] and Sections 1.3.2 and 1.3.3 describe how we estimated the fractional population of the initial rotational and vibrational states for the IR transition (f_{rot} and $f_{v=0}$, respectively), and Table S3 summarizes those estimates for the molecular beams used in this study. We used linearly polarized infrared light to excite the molecular beam, and under those conditions it is possible to excite up to 50% of all molecules in the v"=0, J"=1, K"=0 state. We quantified IR

absorption with our pyroelectric bolometer and varied the incident laser power to obtain the laser-power dependent saturation curve for infrared excitation. We found that the high spectral brightness and intensity of our laser source allowed us to saturate the optical transition for all beams under study, so we take $f_{sat} = 0.5$ for all values of T_n. We then used the calculated values of f_{exc} summarized in Table S3 to calculate the values of $S_0^{\nu_1=1}$ we report in this work.

Our estimates of f_{exc} rely on the similarity of rotational cooling between the CHD_3 and CH_4 isotopologues of methane. To check the validity of those approximations, we compared the pyroelectric bolometer measurements of IR absorption with our prediction of f_{exc}. As noted in Section 1.4, the bolometer is proportional to the flux of CHD_3 molecules in the beam times f_{exc}, the total fraction of those molecules that are excited by the laser. Therefore, the pyroelectric signal may be viewed as a flux-weighted measurement of f_{exc}. We first measured the bolometer signal for IR absorption by CHD_3 with T_n = 300K. Prior studies in our lab indicated that rotational and vibrational cooling are very nearly complete in a 300K nozzle source, and the laser power dependence of the signal shows that the absorption transition is saturated, so $f_{exc} \approx 0.107$. The T_n = 300K measurement links the measured bolometer signal to a known value of f_{exc} that is minimally sensitive to details of the rotational and vibrational cooling dynamics. We then measured the bolometer signal for IR absorption at two additional nozzle temperatures. Figure S3 shows that our predicted values of f_{exc} and the bolometer signal for T_n = 600K and 700K beams differ by 10% or less.

1.5.4 Obtaining $S_0^{\nu=0}$.

Finally, calculation of the state-resolved $S_0^{\nu_1=1}$ requires an estimate of S_0 for the vibrational ground state ($S_0^{\nu=0}$, Eq.S3). Below, in Section 5 we describe three ways in which we have

obtained this estimate. In the main paper, we used the simplest approach and approximated $S_0^{v=0}$ with S_0^{off}, which is an upper bound on $S_0^{v=0}$. This method led to the smallest error bars in calculated values of $S_0^{v_1=1}$. Section 5 outlines two alternative approaches for obtaining $S_0^{v=0}$ that rely on AIMD calculated values for $S_0^{v=0}$. We find that all three approximations of $S_0^{v=0}$ yield similar values for the state resolved reaction probability that differ by less than the error limits on the experimental measurements.

1.6 Impact of surface-bound species on S_0 measurements.

All CHD_3 dissociation measurements described here were performed at a surface temperature of T_s = 550K. We have verified that, for the case of CH_4 dissociation, the H_2 carrier gas does dissociate on the surface at this temperature, but recombinative desorption is prompt and the steady state coverage of H is low. To reach that conclusion, we compared the surface temperature dependence of S_0 for beams of 1% CH_4 in He (E_i = 83 kJ/mol), 11% CH_4 in H_2 (E_i = 105 kJ/mol), and 0.25% CH_4 in H_2 (E_i = 124 kJ/mol). We found that while S_0 for CH_4 in the He carrier beam decreased slowly and monotonically from 0.030 to 0.025 as T_s decreased from 700K to 400K, both H_2 carrier beams showed a sharp falloff in S_0 when T_s dropped below 500K. For example, S_0 for the E_i = 124 kJ/mol beam decreased from 0.07 to 0.006 when T_s dropped from 500K to 400K. However, above T_s = 550K, S_0 for all He and H_2 carrier beams rose slowly and with similar slopes as T_s increased. Ref. [21] provides further details on this measurement and its interpretation. Therefore, the CHD_3 dissociation experiments are performed in the low-coverage limit for H.

Our analysis of the molecular beam reflectivity measurements equates surface uptake of CHD_3 with reaction. If the surface bound methyl and H (or D) reaction products recombinatively

desorbed from the surface promptly, then net uptake would be reduced and our measurements would underestimate the dissociative chemisorption probability. Previously published work indicates that this is not the case. Ceyer and coworkers have shown that the nascent methyl products of methane dissociation on Ni(111) are not hydrogenated by surface-bound H under the conditions of an ultrahigh vacuum surface science experiment [22]. Instead, they dehydrogenate on a 550K surface and the H atoms recombinatively desorb, leaving behind surface-bound C.

In our molecular beam reflectivity measurements of CHD_3 reactivity, we obtain S_0 from the initial drop in CHD_3 partial pressure. During the time of this initial drop, the H atom coverage may be even less that the steady state value, and C has not yet begun to accumulate on the surface. Therefore, we are confident that our measurements yield values of S in the zero-coverage limit for C as well.

1.7 Additional Experimental Considerations

Prior state resolved beam-surface scattering studies show that measuring S_0 at high incident kinetic energy and for high values of S_0, as we do in this study, presents unique experimental challenges. Accessing high kinetic energies (> 100 kJ/mol) requires the use of dilute mixtures of CHD_3 in the lightest possible carrier gas, H_2, as well as elevated nozzle temperatures (T_n).

Equation S3 shows that the state-resolved reactivity is directly related to the absolute difference in reaction probability with and without laser excitation. This difference is very nearly equal to the product of f_{exc} and $S_0^{v_1=1}$. Elevated nozzle temperatures reduce this difference in three ways. First, incomplete rotational and vibrational cooling dilutes the population in the single rovibrational state that serves as the initial state for laser excitation and decreases f_{exc}. Second, as T_n increases, f_{exc} decreases slightly, but S_0^{off} can increase dramatically due to the increased

thermal population of reactive, vibrationally excited states at elevated T_n. When S_0^{off} begins to exceed the product of f_{exc} and $S_0^{v_1=1}$, S_0^{on} and S_0^{off} must each be measured with relative errors of less than 10-20% in order to obtain a meaningful value of (S_0^{on} - S_0^{off}) for use in the calculation of $S_0^{v_1=1}$. Finally, at very high values of E_i, $S_0^{v=0}$, S_0^{off} and $S_0^{v_1=1}$ asymptotically approach and are limited to a maximum value of 1. The additional energy provided by laser excitation can have at most a modest impact on S_0^{off}.

These challenges demand a highly accurate, sensitive and reproducible method for measuring S_0^{on} and S_0^{off} with error bars that are as small as possible, and we use molecular beam reflectivity methods (employing the King and Wells method for detection [20]) to meet this end. Note that using H_2 instead of He as seeding gas helps to reduce the impact of the first two problems mentioned above, as achieving a similar value of the average translational energy requires a lower T_n with H_2 than with He.

2. Theoretical Methods.

2.1 General approach.

We take a semi-empirical approach to constructing and validating a density functional for methane reacting with Ni(111). Four aspects are of particular importance to our strategy.

First, all experiments used are done for a range of incidence energies (E_i) such that the total energy of the molecule (translational + vibrational) is well above the zero-point energy corrected reaction barrier height of the system. This means that the reaction occurs in the classical, "over the barrier" energy regime, which in principle allows the quasi-classical trajectory (QCT) method to be employed (see Ref.[23], and see also Section 2.5 below).

Second, calculations were performed with the AIMD method [23-24], which allows the modeling of all relevant molecular degrees of freedom in addition to the motion of the surface atoms, as known to be important for methane dissociation on metal surfaces [25].

Third, the density functional is constructed using the specific reaction parameter (SRP) approach to density functional theory (DFT) [26] that has previously been applied successfully to the H_2 + Cu(111) [27] and Cu(100) [28] systems. The approach is implemented here by first determining a functional that describes the reaction of methane being mainly in its vibrational ground state at energies above the classical threshold. More specifically, we base the construction of the semi-empirical functional on molecular beam experiments with thermal populations of the molecules such that at least 60% of the molecules are in their vibrational ground state, because we anticipate that the reaction of molecules in CD-bend and CD-stretch excited vibrational states may be described less well with the quasi-classical trajectory method used in the AIMD calculations. Next, the functional is validated, by checking that reaction of methane in a pre-excited vibrational state is also well described.

Fourth, we have selected the CHD_3 isotopologue and its CH-stretch $\nu_1 = 1$ vibrational state to validate the semi-empirical functional, because this combination of vibrational state and methane isotopologue represents a best case for the application of classical dynamics methods (see Section 2.6), as used in AIMD. For instance, the vibrational state selected can be well described at the normal mode level, possessing 95% CH-stretch character [29]. Furthermore, at the ensemble level, energy put into this state in QCT simulations remains localized in this state in gas phase simulations of duration equal to the relevant collision time [30].

For the combination of experimental conditions, methane isotopologue and initial vibrational states selected, the AIMD method represents the method of choice. An advantage over quantum

dynamical methods [31-37] is that motion in all the relevant molecular and surface degrees of freedom is modeled without dynamical approximations. An advantage over QCT calculations employing recently developed force field methods is that no errors are introduced by the need to fit a potential energy surface (this still causes difficulties with describing the molecule-surface interaction at elevated energies [38], and with describing the coupling between molecular and surface atom motion [39]).

A number of other additional aspects are important to our strategy. First, as discussed below in Section 2.2, in our SRP functional we use a correlation functional that approximately describes the van der Waals attractive dispersion interaction. This choice was made because choosing such a functional allows an improved description of weakly activated dissociation problems [40], while highly activated dissociation systems are described at least as well with such a correlation functional as with ordinary (GGA) correlation functionals [41]. In addition, the CH_4 + Ni(111) systems exhibits a van der Waals well (see Section 2.3 and Section 4 below). Second, we make sure that the initial rotational state to which vibrational excitation takes place is taken into account in the AIMD calculations, because quantum dynamical and QCT calculations on the gas phase reaction of Cl atom with CH-stretch excited CHD_3 suggest that it may be important to properly describe the initial rotationally excited state in the calculations ([42], see also Section 2.5 below). Third, reaction probabilities for the molecule in its excited vibrational $\nu_1 = 1$ state were measured for a large range of incidence energies (112-160 kJ/mol), enabling a more rigorous validation test than was possible before, where these data were available over a much more limited range of total energies above the zero-point energy corrected minimum barrier height for CHD_3 + Pt(111) (i.e., for E_i = 38.3 - 49.6 kJ/mol, see Table S1 of Ref.[23]).

Continuing with our assessment, fourth, the experiments and calculations were done for a high surface temperature (550 K), which is well above the surface Debye temperature of Ni(111) (370 ± 5K [43]), suggesting the applicability of classical mechanics to the simulation of the surface atoms (see also Section 2.5). In contrast, previous state-resolved experiments on CHD_3 + Pt(111) were performed for a much lower surface temperature (120 K [23], close to or below the surface Debye temperature of Pt(111), which is estimated to be between 111 and 143 K [44-46]). To allow the use of higher surface temperatures, as described in the previous section reaction was measured using a beam reflectivity technique [20]. Fifth, as already alluded to all experiments were performed using H_2 as a seeding gas. This allows high average collision energies to be achieved with the lowest possible nozzle temperature, in contrast to experiments using He as seeding gas; the latter would require nozzle temperatures in excess of 900 K to achieve average incidence energies ≥ 100 kJ/mol (see Fig.S4). Seeding with H_2 has the advantage that, at comparable incidence energies, the vibrational temperature of CHD_3 in laser-off experiments using H_2 as seeding gas is lower, meaning that the vibrational state population is dominated by the ground state to a larger extent (see also Fig.S4). This is favorable to the application of the QCT method implicit in the use of AIMD, which we anticipate to be less accurate for CD bending and stretch excited states. In contrast, previous calculations of CHD_3 + Pt(111) had to rely on laser-off experiments using He seeding to achieve collision energies in the energy range just above the barrier for this system (i.e., 75.4 - 84.4 kJ/mol), making these experiments [23] less useful for devising an SRP functional than they could have been [47]. Sixth, unlike for CHD_3 + Pt(111) [47] the finite initial interaction of CHD_3 with the surface at the start of the trajectories was taken into account in such a way that its effect on the SRP functional is described, as detailed below. The last five aspects all represent improvements over a very recent attempt at deriving a SRP density

functional for reaction of methane on Pt(111), which led to a better description of reaction than achieved with the PBE functional, but not yet to a chemically accurate description [47].

In the dynamical model described below we take into account the possibility of energy transfer to the surface vibrations (phonons), but we neglect the possibility of electron-hole pair (ehp) excitation, for two reasons. First, as will become clear below the CH_4 + Ni(111) system exhibits a physisorption well with a well depth of only 12 - 20 kJ/mol, and no deep molecular chemisorption well at the gas phase side of the barrier. A consideration of experiments performed by Nienhaus and co. [48] then suggests that the molecule should not dissipate energy through ehp excitation when moving through this well to the barrier. Second, the CH_4 + Ni(111) system exhibits a large difference between the work function of the metal and the electron affinity of the molecule (see Fig.2 of Ref. [49]), because Ni(111) has a high work function (516 kJ/mol)[50] and CH_4 a negative electron affinity, i.e., the uptake of an electron by CH_4 is endothermic [51]. This rules out efficient electron transfer from the metal to the molecule, which can drive electron hole-pair excitation and even electron emission, as shown by experiments performed by Wodtke and Auerbach and co-workers [52]. Calculations on H_2 + Pt(111) [53] have also suggested that ehp excitation is not important for the reaction in systems characterized by a low electron affinity of the molecule (< -300 kJ/mol for H_2 [54]) and a high work function of the metal (550 kJ/mol for Pt(111) [50]). The above evidence suggests that ehp excitation should not have a considerable effect on sticking of methane to Ni(111).

Recently, Jiang et al.[55] have performed molecular dynamics with electronic friction (MDEF) calculations on dissociative chemisorption of H_2O on Ni(111) to address how inclusion of ehp excitation in the model might affect the sticking of H_2O and D_2O. For the range of E_i of 100-125 kJ/mol they studied that overlaps the range of E_i relevant to our work (100-160 kJ/mol),

vibrational ground state sticking probabilities appear shifted to higher E_i by about 1 kcal/mol for H_2O, and 0.5 kcal/mol for D_2O (see figure 2 of Ref.[55]). If a similar shift would apply to our calculations for CHD_3 + Ni(111) as for H_2O + Ni(111), our electronically adiabatic calculations with the SRP-DFT-AIMD procedure might lead to an overestimate of the reaction barrier height by about a kcal/mol, which is the accuracy we seek (chemical accuracy).

However, we believe that, if one would use the same local density friction approximation (LDFA) model as used by Jiang et al., which uses the so-called independent atom (IAA) approximation (Ref. [55] and references therein), for CHD_3 + Ni(111) the actual shift in the sticking probability should be smaller for the energy range discussed by probably at least a factor two, for two reasons. First of all, as discussed in the main paper the value E_b of the barrier height we derive for methane + Ni(111) is 98 kJ/mol. This is much higher than the value of E_b associated with the H_2O + Ni(111) PES, which is only 65 kJ/mol with the PES Jiang et al. used[56]. This means that, near the barrier, the available center-of-mass translational energy (or, alternatively, the energy in the reaction coordinate) should be much higher for H_2O + Ni(111) (by about 33 kJ/mol) than for CHD_3 + Ni(111), for similar E_i (between 100-125 kJ/mol). This suggests that less energy should be dissipated to ehp for the latter system, as the rate of this energy dissipation, λ, should be proportional to the available energy, E_{av}. Specifically, ($\lambda = -2 \langle\eta\rangle E_{av}/m$)[57], where $\langle\eta\rangle$ is the average friction coefficient experienced, and m is the relevant mass, i.e., the mass of the molecule. The mass of CHD_3 (19 amu) is similar to that of H_2O (18 amu). Energy loss to ehp should be dominated by the friction experienced by the hydrogen atom closest to the surface, which can get much closer to the Ni surface in the transition state in both H_2O + Ni(111) (see figure 1 of Ref.[55]) and CH_4 + Ni(111) (see Fig.2 of main paper) than the O or C atom and the other hydrogen atoms, and which is actually at similar distance to the Ni(111) surface for both

transition states (see Ref.[55] and Fig.2). It follows that in H_2O + Ni(111) more energy should be lost from the COM motion to ehp excitation than for CHD_3 + Ni(111), because the available COM translational motion is higher near the barrier for the former system, while similar average friction coefficients should be sampled, and the mass of the molecule is likewise similar.

The second reason concerns energy dissipation from the molecular vibrations to ehp excitation. An issue not discussed in Ref.[55] is whether the shift in the sticking probability for H_2O + Ni(111) is mostly due to this energy dissipation mechanism, or to the previously discussed energy dissipation from the COM motion to ehps. The difference between the energy shift noted above for H_2O (about 1 kcal/mol) and D_2O (about 0.5 kcal/mol) suggests that an important part of the energy shift observed in the sticking probability when taking electronic friction into account comes from energy dissipation from the vibrations. This might seem surprising given the high incidence energy. However, the "mass" or reduced mass associated with OH stretch vibrations taken in the local mode picture (which works quite well for H_2O) is, at about 1 amu, much less than the mass of the COM (about 18 amu). From the zero-point energy of H_2O and subtraction of the part due to the bending mode, each OH stretch vibration has about 23 kJ/mol of zero-point energy[58]. For a harmonic oscillator, the energy dissipation rate from a single stretch vibration is then given approximately as $\lambda = - <\eta> E_{av}/m$ [57] $\approx - 23 <\eta>$. The dissipation rate from the COM motion is, taking E_{av} equal to the highest value of E_i considered in Ref.[55] (125 kJ/mol), given by $\lambda = - 2 <\eta> E_{av}/m \approx - 14 <\eta>$. This simple back of the envelope calculation suggests that, in H_2O + Ni(111), energy dissipation from vibrations might well be equally or more important in diminishing the sticking than energy dissipation from the COM translation to ehp excitations. Comparing CHD_3 + Ni(111) to H_2O + Ni(111), in view of the already mentioned similarities between the transition states (see Figure 2 of main paper and figure 1 of Ref. [33], and the fact that

for both systems the dissociating hydrogen atom can get much closer to the surface than the C or O atom and the other hydrogen atoms and thereby experience much higher friction forces[55], the following might then be said.

For CHD_3, in view of the statistical bond breaking observed in experiments and also seen in our calculations for laser-off reaction, the dissociating hydrogen atom should be a D-atom in 75% of the reactive events, while in H_2O dissociation it is always the faster moving H-atom. It is therefore plausible that, as far as the hindering of reaction by dissipation of vibrational energy to ehps in concerned, CHD_3 + Ni(111) should be more like D_2O + Ni(111) than like H_2O + Ni(111), and this also suggests a smaller shift of the reaction probability curve due to ehp excitation for CHD_3 + Ni(111) than obtained with LDFA/IAA theory for H_2O + Ni(111).

The above is not the complete story about energy dissipation due to ehp excitation. For example, it is wholly unclear whether MDEF with friction calculated using the LDFA in the IAA can correctly describe energy dissipation from vibrations to ehp excitation. Obviously, in the molecule travelling to the surface the energy in the vibrations need to remain quantized in some approximate sense. This may entail that energy should be dissipated simultaneously to the electrons and to COM translational motion. If this is to be mediated by electronic friction, off-diagonal friction coefficients are needed in tensorial friction coefficients[59]. These are usually much smaller than the diagonal friction coefficients, which are more comparable to the LDFA friction coefficients[59]. This might then suggest that the LDFA/IAA model used by Jian et al. for H_2O + Ni(111) could well overestimate the effect of energy dissipation to ehps on the sticking in this system. On the other hand, it is also possible that the neglect of the molecular electronic structure (which can be taken into account in models using tensorial friction[59], but not in the LDFA/IAA model) could lead to the effect of ehp excitation on the sticking being

underestimated[60] in the work on H_2O + Ni(111). We conclude that our procedure for obtaining an SRP density functional, and the accuracy of the minimum barrier extracted for reaction, does depend on whether the electronically adiabatic approach taken here is accurate. However, we argue that the accuracy of our approach for CHD_3 + Ni(111) is not invalidated by the results of Jiang et al. for H_2O + Ni(111), for the reasons discussed above. In future, accurate MDEF calculations on CHD_3 + Ni(111) using, ideally, tensorial friction will hopefully shed further light on this issue.

2.2 Construction of the SRP density functional.

Regarding the exchange-correlation functional used in the AIMD, a variant of the SRP approach originally proposed by Truhlar and coworkers [26, 61] has been implemented. This choice was made because in general quantitative accuracy is not within reach with the use of density functionals on the "lower rungs of Jacob's ladder" (i.e., with standard functionals within the generalized gradient approximation (GGA) or meta-GGA, with "standard" meaning that they have not been semi-empirically adapted for the description of one specific system) [62]. For example, the average of the mean unsigned error for gas phase reaction barrier heights computed [63] for the HTBH38/08 and NHTBH38/08 databases is 8.9 kcal/mol and 6.6 kcal/mol (37 and 28 kJ/mol) for the PBE [64] and RPBE [65] GGA functionals, respectively. We have therefore resorted to the use of a semi-empirical density functional, but in defining this functional we have built as much as possible upon constraint-based, non-empirical functionals. This was done to ensure that the functional constructed is valid over a large range of coordinate space, and to aid is applicability to other molecules interacting with metal surfaces.

To obtain the exchange-correlation functional, the exchange functional was taken as:

$$E_x = x \cdot E_X^{RPBE} + (1-x) \cdot E_X^{PBE} \qquad \text{(S5)}$$

where E_X^{RPBE} and E_X^{PBE} are the exchange terms in the RPBE [65] and the PBE [64, 66] exchange-correlation functionals, respectively. Formally, the use of Eq.S5 has the advantage that all constraints imposed on the PBE exchange functional considered by itself are still in place, as Hammer et al. made sure these constraints were maintained in their modification of the PBE functional (RPBE) [65]. The constraints include the spin-scaling relationship, the Lieb-Oxford bound, and, importantly, the recovery of the uniform gas limit (Ref.[64] and references therein), which ensures the functional's applicability to metals [62]. Combining Eq.S5 with the standard PBE correlation functional [64] also used in RPBE [65] has an important practical advantage in describing activated dissociative chemisorption problems: for most molecule-metal surface systems we are aware of, dynamics calculations performed with an appropriate level dynamical model show that using PBE leads to an underestimate of the minimum reaction barrier height, while using RPBE leads to an overestimate. This can be seen from research on H_2 + Cu(111) [27, 67], H_2 + Cu(100)[28], H_2 + Ru(0001) [40, 68-69], D_2O + Ni(111) [33], and CHD_3 + Pt(111) [47], noting that PW91 [70] and PBE [64] can be used almost interchangeably [64]. The above conclusion holds regardless of whether PBE or vdW-DF correlation is used. Research on NH_3 production, which showed that better production rates could be obtained by taking weighted averages of PW91 and RPBE energies [71], also helped guide us originally [27] with the choice of Eq.S5. In other words, by interpolating the exchange between two equally justifiable, constrained density functionals at the GGA rung, i.e., between the general purpose PBE functional [62, 64] and the RPBE functional that is better at describing chemisorption energies [65], it should be possible to reproduce the minimum barrier height for many systems, and to improve the description of heterogeneously catalyzed processes.

In preliminary AIMD calculations we have used the correlation part of the PBE exchange-correlation functional [64], which has been taken over in the RPBE functional [65]. At a later stage,

we have switched to using the correlation functional of Dion et al. (referred to as vdW-DF here) [72]. Formally, this choice can be justified on several grounds. First, the functional is non-empirical, being based on first principles [73]. By construction, the functional recovers the uniform electron gas limit [72], again ensuring its applicability to metals. While it is still approximate, unlike the semi-local GGA-level correlation functionals the vdW-DF correlation functional additionally allows for a reasonably accurate description [74] of the van der Waals dispersive forces [75]. In this framework, the non-local part of the functional ensures an asymptotically correct description of the molecule-metal surface interaction [72]. The vdW-DF functional [72] has been designed to function as a general purpose correlation functional [73], i.e., to describe London dispersion forces *in addition* to the effects that are described by GGA type correlation functionals, such as the PBE correlation functional. When matched with an appropriate exchange functional [76], its use allows an accurate description of a range of problems affected by competing interactions [77].

There are also important practical advantages to using the vdW-DF correlation functional. For instance, previous experience suggests that using this correlation functional instead of PBE correlation allows an improved description of weakly activated H_2 dissociation problems [40], while highly activated H_2-metal surface dissociative chemisorption systems are described at least as well [41]. Perhaps more importantly, the use of vdW-DF correlation also allowed a better description of dissociative chemisorption in the CHD_3 on Pt(111) system [47], that is very similar [78] to the CHD_3 + Ni(111) system considered here.

In the past there has been some ambiguity concerning which exchange functional best to match the vdW-DF correlation functional with, with the use of the revPBE functional [79] to which vdW-DF was originally coupled [72] leading to underbinding of van der Waals dimers [74]. However, here

the use of Eq.S5 actually becomes a practical advantage, as research has shown that interpolating between PBE and revPBE (with revPBE [79] being very similar to RPBE [65]) in the functional called PBEκ=1-vdW leads to much higher accuracy (chemical accuracy in the more favorable cases) for the S22 van der Waals molecules database than achievable with revPBE-vdW-DF and PBE-vdW-DF, with the latter combination being systematically overbinding[74]. The use of an exchange functional that may be viewed as interpolating between PBE and RPBE (i.e., the optPBE exchange functional[74]) with vdW-DF leads to even higher accuracy on the S22-database. Also, the use of optPBE-vdW-DF leads to reasonably accurate results for solid state materials, with this functional exhibiting similar or better accuracy for lattice constants and atomization energies than PBE[80]. Additionally, the use of optPBE-vdW-DF leads to comparable [81] or better [82] results for chemisorption energies of atoms and molecules on late transition metals than the PBE functional. Combining vdW-DF correlation with a mixture of PBE and RPBE exchange does not lead to the cancellation of semi-local exchange and correlation in the limit of small density gradients, as the combination with PBE correlation would [64], but this is not a major concern [83]. Also, as pointed out above various combinations of vdW-DF correlation with exchange functionals have shown high accuracy for van der Waals interactions, but none of these obeyed the constraint that vdW-DF correlation should cancel the semi-local exchange contribution in the limit of small density gradients.

In summary, the use of vdW-DF also has many practical advantages. Other approaches exist that may be competitive in terms of accuracy for van der Waals bound systems, like the version of the Tkatchenko-Scheffler method specialized to the description of hybrid inorganic-organic systems [84-85] and methods using the random phase approximation (RPA) [86-87]. We have refrained from using the former as this would add another semi-empirical parameter to our approach, i.e., a

scaling coefficient required to describe the function that damps the van der Waals dispersive term [85, 88], while AIMD calculations using RPA correlation would presently be computationally intractable due to unfavorable scaling with the number of electrons [62].

Our reasons for adopting the specific semi-empirical exchange-correlation functional described above may then be summed up as follows. First, semi-empiricism is presently unavoidable if chemical accuracy is sought for the systems of interest (molecules reacting on metal surfaces). While Perdew et al. [62] recommend the use of semi-empiricism to functionals of the fourth rung (hyper-GGA or hybrid) and higher, for our systems this is not an option since adding the required exact exchange would make AIMD calculations intractable due to unfavorable scaling of computational cost with the number of electrons [62]. Furthermore, adding exact exchange to the functional has no proven advantages for molecules interacting with metal surfaces [89-91]. Descending to the lower meta-GGA rung, we find that the constrained "non-empirical" versions do not have much to offer in improved accuracy beyond allowing a somewhat more accurate prescription of the metal surface [62], as also suggested by a recent study on H_2 + Ru(0001) [40]. Additionally, we are not aware of a pair of well-constrained meta-GGA functionals of which the application would bracket the reaction barrier height for the systems of interest, like PBE and RPBE at the GGA rung. We therefore use the rung 2 exchange functionals present in the PBE and RPBE exchange-correlation functionals. For reasons discussed above, we use vdW-DF correlation instead of the standard PBE correlation. While arguments may undoubtedly be advanced against the approach we take, we think it is the currently best approach using a single adjustable parameter in a well motivated and constrained functional, within a computationally tractable AIMD framework. The bottom line of why we use it is that it has proven accuracy for

H_2-metal systems [40-41] and CH_4 + Pt(111) [47], and, as we will show in the present work, also allows a chemically accurate description of methane dissociation on Ni(111).

2.3 Electronic structure calculations.

All the AIMD and electronic structure (density functional theory, DFT) calculations have been performed with the VASP code (version 5.3.5) [92-96]. A basis set including plane waves up to a kinetic energy of 350 eV (1 eV ≈ 96.485 kJ/mol) has been employed. In order to facilitate convergence, a Fermi smearing with a width parameter of 0.1 eV (9.6 kJ/mol) has been applied. Core electrons have been represented with the projector augmented wave (PAW) method [96-97], using an Ar core PAW pseudo-potential for Ni. The Ni-surface is modeled with a 3 x 3 surface unit cell and a 4-layer slab, with the slab separated from periodic images by a vacuum distance of 13 Å in the supercell approach used. The first Brillouin zone has been sampled with a Γ-centered 4x4x1 k-point grid. Spin polarized calculations have been performed, as suitable for magnetic materials like Ni.

Tests confirmed that the DFT setup used above yields a high enough accuracy for the interaction of methane with Ni(111). This was established by convergence tests on the molecule surface interaction energy using an ideal Ni(111) slab, in which the Ni atoms are constrained to remain in their equilibrium positions. The tests used the lowest transition-state (TS) geometry determined by Nave and Jackson (C2 geometry in Refs. [98-99]), and the PBE functional (also employed in Refs. [98-99]), but the same convergence behavior is expected for slightly different barrier geometries and other exchange-correlation functionals, like the SRP32-vdW functional used here and discussed and defined below. The barrier energies reported in Table S4 have been calculated as $E_b = \varepsilon_b - \varepsilon_{asym}$, where ε_b and ε_{asym} are the absolute (DFT) energies calculated for the

barrier geometry and for the asymptotic configuration, in which the molecule is in its equilibrium gas-phase configuration and placed midway between two periodic replicas of the slab, respectively.

Table S4 clearly shows that our computational setup returns a E_b value that does not differ by more than 0.8 kJ/mol from the most converged values with respect to plane-wave cutoff energy, the number of k-points, the surface unit cell size and the number of atomic layers. Our finding that the use of a 3 x 3 surface unit cell and a 4 layer slab is sufficient to achieve convergence of the barrier height to within chemical accuracy (1 kcal/mol ≈ 4.2 kJ/mol; with this accuracy the rate of an activated reaction is uncertain to within a factor 2 or less at typical temperatures relevant to heterogeneous catalysis (≥ 700 K)) is corroborated by plane wave DFT calculations [100] performed with the very similar PW91 functional [70] (see also Table S4, noting that the PW91 and PBE energies are very similar, as the PBE functional was constructed with one of the aims being to reproduce PW91 energies [64]). Our results are also consistent with the PBE result of Ref. [36], which agrees with our results for the 3 x 3 surface unit cell and the 4-layer slab to within 2.1 kJ/mol. This is especially true if one takes into account that the calculation of Ref. [36] was done for a geometry much like the B1 geometry of Ref. [98], which should result in a barrier height that is about 1 kJ/mol higher than that of the C2 geometry that we use, according to the results of Ref.[98]. The comparison of our PBE barrier height to those of Ref. [98] and of Refs. [31, 101] shows that the use of a 2x2 surface unit cell is, however, not enough to achieve such convergence, the 2x2 results differing from the 3x3 results by about 8 kJ/mol (see also Table S4).

When employing 30 Å of vacuum space, at Z = 6 Å, the distance from the surface at which the methane molecules are initially placed when simulating the molecule-surface collisions, the interaction energy is about 4 kJ/mol with the SRP32-vdW functional (Fig.S5). Considering the

fact that the molecule-surface interaction at $Z \geq 6$ Å is independent of the molecular coordinates other than Z, we can mimic the effect of the molecule's interaction with the surface that is already present at Z = 6 Å by adding 4 kJ/mol of energy to the translational motion of the molecule towards the surface. This allows us to perform the expensive AIMD calculations described below with a computationally much cheaper setup (i.e., one using a vacuum spacing between the Ni(111) slabs of 13 Å, rather than a much larger vacuum spacing).

Using the described computational setup, bulk calculations performed within the primitive unit cell for a fcc lattice and using the SRP32-vdW functional (i.e., Eq.S5 for the exchange functional and vdW-DF for correlation [72], with x = 0.32 as turned out to be optimal, see Section 2.2 and Section 4), returned an equilibrium lattice constant a_L = 3.556 Å for Ni. This value is in reasonable agreement (to within 1.2%) with the low-temperature (10 K) experimental value a_L=3.513 Å [102]. Based on the convergence tests described above, the Ni surface has been modeled with a 4 layer slab within a 3x3 supercell, the interlayer distances of which have been optimized.

2.4 Determination of the transition state.

In order to identify the minimum energy barrier in the multidimensional PES that describes the dissociation of methane on Ni(111), we have performed climbing image nudged elastic band (CINEB) calculations using the transition state tools package as implemented in VASP by Henkelman and Jónsson [103-104]. Four images have been employed to sample the reaction path connecting the reactant state (in which a methane molecule was placed at Z = 4 Å, with subsequent geometry optimization of CH_4 relative to Ni(111)) to a product state, corresponding to the optimized geometry of a methyl fragment and an H atom adsorbed in different configurations on the Ni(111) surface. The four paths differing in the product state geometry as found by Nave and Jackson [98-99] to correspond to the lowest reaction barriers have been

considered here. An ideal slab has been employed for the CINEB calculations, constraining the surface atoms to remain in their equilibrium positions. The images have been optimized until the forces acting on all the atoms became smaller than 10 meV/Å (≈ 1 kJ mol^{-1} $Å^{-1}$). We have verified that the image with the highest energy in each CINEB calculation corresponds to a first order saddle point in the multidimensional PES through a frequency analysis (by demanding that only one imaginary frequency is found).

2.5 AIMD calculations.

In order to account for surface temperature effects in the AIMD calculations, a procedure analogous to the one employed in Refs. [23, 67] has been employed. Initial displacements and velocities have been assigned to the surface atoms of the first three layers according to an independent harmonic oscillator model to mimic local distortion of the ideal surface and thermal motion of the surface atoms. The frequencies employed in this model are derived from normal mode calculations for a single Ni atom in an ideal slab, which have been performed for each of the atomic layers. Such calculations returned frequencies in the range $1.8 < \omega < 2.3$ kJ/mol. An expanded lattice constant (1.0077 times the theoretically computed value of a_L) has been employed to construct the slab in order to account for the experimental thermal expansion [102] of the metal from 0 K to the experimental surface temperature that we want to mimic, i.e. 550 K. Ten differently-initialized slabs generated in this way have been equilibrated for 2.5 ps with NVE (constant number of particles N, volume V and total energy E) AIMD runs and a time-step equal to 1 fs, allowing the atoms in the uppermost three layers to move. The configurations (positions and velocities) assumed in the last picosecond by the Ni atoms during these clean-surface equilibration runs (1000 configurations for each of the 10 differently initialized surfaces) have been employed to form a pool of configurations from which the initial conditions of the

surface atoms in the molecule-surface collision runs have been sampled. The average surface temperature computed across all these configurations is 537 K, with a standard deviation σ = 73 K.

As already mentioned in Section 2.1, a high T_s was selected in both the experiments and the calculations, to ensure applicability of the quasi-classical trajectory method. As also noted above, the selected T_s (550 K) is in excess of the Debye-Waller temperature of Ni(111) (370 ± 5K[43]). For values of T_s higher than the Debye-Waller temperature the validity of a classical approach to dynamics calculations on scattering from a surface can be assessed by computing the argument to the Debye-Waller factor, which is given by [105]

$$2W = \frac{3p^2 T_s}{M_C k_B \Theta_D^2}, \qquad \text{(S6)}$$

where p^2 is the average of the square of the change in momentum of a scattering molecule, M_C the mass of a surface atom, k_B the Boltzmann constant, and Θ_D is the surface Debye temperature. Experience suggests that treating the surface vibrations classically works well for $T_s > \Theta_D$ for values of 2W greater than 6 [106-107] (note that 2W is a dimensionless quantity). For methane scattering from Ni(111) at one but lowest E_i investigated under laser-off conditions (112 kJ/mol), our calculations show a value of about 360 for the Debye Waller argument 2W. Clearly, under the conditions we investigate the energy transfer to the surface is in the classical regime, and can be described with classical mechanics.

Another important reason for taking $T_s > \Theta_D$ is that the vibrational motion of the surface atom above which methane dissociates modulates the barrier height for dissociative chemisorption on Ni(111) [25, 98]. In this case a classical description of the phonons as vibrations at low surface temperatures should be avoided, because textbook chemical physics shows that quasi-classical

and quantum descriptions of vibrational motion radically differ on the probability of finding an oscillator close to its classical turning point in the quasi-classical and the quantum description of the vibrational ground state. Taking $T_s > \Theta_D$ avoids this problem as at such surface temperatures most of the surface atom vibrations will be in excited states. While it might be preferable to extract a barrier height for methane interacting with a static surface from a calculation with as low a surface temperature as is possible experimentally, such an approach is incompatible with the use of classical mechanics, and quantum dynamics calculations still require drastic approximations to both molecular motion and surface atom vibrations, as emphasized in the main paper. While the surface atom vibrations should influence the average barrier height experienced by the molecules for a given T_s, this effect should be properly described with classical mechanics for $T_s > \Theta_D$. As quantum dynamical calculations are presently impossible without drastic approximations, we accept that the experiments and calculations have to be performed for $T_s > \Theta_D$. In the context of the present comparison to experiments this is necessary anyway, as $T_s \geq 550$ K was required to ensure the measurement of sticking probabilities in the limit that the surface was not pre-covered by hydrogen, as could otherwise occur with the use of beams with seeding in H_2 (as required for achieving high E_i, see also Section 2.1).

The sticking probability has been calculated by computing 500 NVE trajectories for each of the simulated molecular beam experiments. The number of trajectories has been doubled for the simulation of molecular beams characterized by the lowest reaction probabilities ($S_0 < 0.08$). The Verlet algorithm as implemented in VASP with a time step of 0.4 fs has been employed to integrate the classical nuclear equations of motion. The molecules are initially placed at 6 Å from the surface, with their center of mass randomly sampling an impact point in the supercell plane. The initial velocity of the molecule towards the surface samples a flux weighted velocity

distribution of the form of Eq.S1 (see also Ref.[10]), in which the values of the stream velocity v_0 and the width parameter α have been obtained by fitting the analogous expression for flight times to recorded time-of-flight spectra of the beams used in the present study (See Section 1.3.1 and Table S1). As already noted above, for each trajectory the velocity towards the surface was then increased to effect an increase of the collision energy by 4 kJ/mol, to mimic the effect of the molecule's initial interaction with the surface at Z = 6 Å (see Sections 2.1, 2.3, and Fig.S5). Correcting for the finite van der Waals interaction at the start of the trajectory in this way represents an improvement over a very recent attempt at deriving a SRP density functional for reaction of methane on Pt(111), which was only partially successful [47]. The translational energy of the molecules in the direction parallel to the surface is set to zero, to simulate molecular beam experiments performed at normal incidence.

The QCT method has been implemented here, meaning that vibrational ZPE has been initially imparted to the CHD_3 molecules. When simulating laser-off beams, the initial vibrational state of the molecules is sampled from a Boltzmann distribution as calculated for the experimental nozzle temperature. To simulate the laser-off experiments the angular momentum of the molecules has been initially set to zero, and the molecule's orientation has been sampled from a random distribution. For simulating the laser-off reaction this should be a good approximation, as experiments have shown that the reaction of CH_4 (which should be similar to that of CHD_3 when considering the vibrational ground state) is essentially independent of the rotational state for typical rotational temperatures of methane molecular beams [6], and the rotational temperature of the beams employed is quite low (see Section 1.3.3 and Table S3).

For calculating the reaction probability for the ν_1=1 vibrational state, only molecules in this state have been simulated. Experimentally, the ^{0}R(1) transition has been employed to excite the

molecules to the vibrationally excited state, selectively preparing molecules in the v_1=1,J=2,K=0 state (see Section 1.4). Even though a linearly polarized laser has been employed to excite the molecules, the excitation occurs at a relatively large distance from the surface (the flight time of the molecules from the excitation region to the surface is >100 μs) so that the hyperfine coupling should erase any possible initial rotational alignment [108]. We have therefore simulated a statistical distribution of M states (M=±2,±1,0) in the simulations of the CH-stretch excited beams.

Based on the above considerations, to compare with the measured $S_0^{v_1=1}$ we describe the initial rotational state in which the molecules are prepared experimentally in the following way in our AIMD simulations. First, the angular momentum vector, the magnitude of which is fixed according to the J quantum number ($|\boldsymbol{J}|=\hbar[J(J+1)]^{1/2}$) given by J = 2, is oriented in the figure axis reference frame in such a way that it forms an angle $\chi=arcos(K/[J(J+1)]^{1/2})$ with the figure axis [109-110], where K is taken equal to zero. Next, the figure axis reference frame is rotated so that the angular momentum forms an angle with the space-fixed z-axis (chosen to coincide with the surface normal) equal to $\xi=arccos(M/[J(J+1)]^{1/2})$. This reflects the quantization of the projection of the angular momentum on a space-fixed Z-axis (M being the corresponding quantum number). Note that quantum dynamical and QCT calculations on the gas phase reaction of Cl atom with CH-stretch excited CHD_3 have shown that it may be important to describe the initial rotational state excited to experimentally in the calculations [42].

The parameters that have been employed to simulate the beams are reported in Table S1. The error bars associated with the theoretical reaction probabilities represent 68% confidence intervals and have been estimated according to the Wilson (or score) method [111].

In our AIMD calculations, a molecule is considered reacted if one of the CH bonds becomes larger than 3 Å, or it becomes larger than 2 Å and it retains such a length for more than 100 fs. A

molecule is considered scattered if its center of mass reaches a distance of 6 Å from the surface with the velocity pointing away from the surface. The trajectories are propagated until one of these outcomes is reached. In very few cases (2 trajectories out of more than 7000 simulated) the molecule remains trapped in the physisorption well after the impact with the surface. If, after propagating these trajectories more than 1 ps, none of the previously described outcomes is observed, we consider these trajectories as scattered. Also in very few cases (5 trajectories in total), we observe an almost simultaneous breaking of two CH bonds of the molecule upon the impact on the surface, leaving two H atoms and a CH_2 group adsorbed on the surface. Such trajectories are considered reacted, which is in accordance with how the sticking of CHD_3 is measured experimentally (such an event would contribute to the pressure drop measured in the King and Wells method [20] and used to determine the dissociation probability, see Section 1.5.1).

2.6 Quality of the QCT method for comparison with present experiments.

The QCT method should be quite suitable for accurately describing most of the experiments presented here. As also discussed elsewhere [23], calculations on D_2 + Cu(111) showed that, if all molecular degrees of freedom are included in the dynamics calculations, QCT calculations essentially reproduce quantum dynamics results for translational energies just above the zero-point energy corrected minimum barrier height [112]. QCT calculations on D_2 + Cu(111) also excellently described the difference in reactivity between molecules in their ground (v=0) and vibrationally excited (v=1) states [112]. As the frequency of the ν_1=1 CH-stretch vibration (≈2990 cm^{-1} [58]) is very similar to that of D_2 (which has a harmonic frequency of 3118 cm^{-1} [113]) and the associated reduced masses are also very similar (≈ 1 a.m.u), it is quite likely that the same is true for CHD_3. Furthermore, we [23] and others [30] have shown that the reaction of ν_1=1 CHD_3 is unlikely to be affected by artificial energy transfer from the initially excited CH-stretch vibration

to the other vibrational modes in the isolated molecule, even though such transfer is in principle possible in classical mechanics. In this connection it is important that, for all the collision energies considered here, our calculations suggest that the reactivity of ν_1=1 CHD_3 is dominated by CH-bond breaking. For instance, at the nozzle temperature of 750 K, more than 2/3 of the molecules that react do so by breaking their vibrationally excited CH-bond.

There is considerable evidence that for the conditions we address the QCT approach is not invalidated by problems related to zero-point energy violation, or the neglect of tunneling. Previous AIMD calculations on dissociation of CHD_3 on Pt(111) concluded that, even on a cold surface (120 K), no proof of zero-point energy violation could be found for reaction at an average translational energy just above the zero-point energy corrected barrier height [23]. As was also discussed already in Ref. [23], the overestimation of the vibrational ground state and laser off reactivity of CH_4 on Ni surfaces obtained with the QCT method for low E_i by Mastromatteo and Jackson [114] can be attributed to dynamical approximations to the molecule's translational and rotational degrees of freedom. Specifically, they used the rotationally adiabatic approximation for treating the rotations[114], which is similar to keeping the orientation of the molecule fixed to its most favorable orientation while the molecule travels along the reaction coordinate. In the comparison of quantum dynamics to QCT results that comes closest to being full-dimensional and to using the same dynamical model, which was made for H_2O dissociation on Ni(111), the QCT and quantum dynamics results were consistent with the QCT results being accurate for reaction probabilities ≥ 0.01 (see figure 7 of Ref.[115]). In these calculations, the static surface approximation was made to the Ni(111) surface, and the QCT calculations treated all nine molecular degrees of freedom. Furthermore, the only approximations made in the quantum dynamics calculations were that the calculations were done for fixed sites and, for each site, for a

fixed azimuthal angle for rotation of the molecule about the surface normal, with subsequent averaging over the reaction sites.

Concerning tunneling, as also discussed before in Ref. [23], already for reaction probabilities as low as 10^{-3} and surface temperatures as low as 120 K tunneling is expected to have very little effect on the reaction of methane on a Ni surface. One reason that tunneling should not have an important effect on reaction of methane on Ni surfaces is that both the dissociating H-atom and the methyl fragment have to move away from the transition state geometry in order to react, leading to a large tunneling mass [98].

A caveat is in order for the simulation of the reaction of CHD_3 in the laser-off experiments at higher nozzle temperatures ($T_n \geq 700$ K). At these temperatures there is considerable population of the CD-bend and CD-stretch excited vibrational states, and it is not certain that the reaction of CHD_3 in these states is correctly described with classical mechanics. We expect our QCT calculations for laser-off reactivity to be most accurate for the lowest nozzle temperatures considered here ($T_n \leq 650$ K). Under these conditions, on the one hand the collision energy is well above the zero-point energy corrected barrier height (see Tables S1 and S6), while on the other hand the CD vibrational bend and stretch states are not yet highly populated (the vibrational ground state population exceeding 60%).

Regarding the accuracy of the QCT method, it was recently noted that the vibrational efficacies computed for CH_4 + Ni(111) with QCT using a 12-dimensional (12D) model were generally lower than the values obtained with an 8-dimensional (8D) quantum dynamical (QD) method [116], and a statement was made [116] that a similar difference had been noted for a gas phase reaction, i.e., of H with HOD[117]. There are, however, several problems with this comparison, and with this statement. First, problems with the QCT-QD comparison made for methane reacting on

Ni(111) were that different dynamical models were used in the QCT and the QC calculations, and that the calculations were performed for CH_4. Obtaining accurate results for this methane isotopologue should be much more challenging for classical mechanics than for CHD_3, due to the possibility of resonant coupling between CH-stretches and bends. Second, in the paper on H + HOD the authors emphasized that the comparison of the QD results to results obtained with other theoretical methods (such as QCT) should not be viewed as a very strict comparison, which should be due to, for instance, differences in the potential energy surfaces employed in the calculations[117]. Third, it is possible to provide a counter example for a gas phase reaction that is much more similar than the CHD_3 + Ni(111) reaction under study here than the H + HOD reaction. Specifically, full-dimensional QCT results for the initial-state resolved cross section for reaction of $O(^3P)$ with CH_4 were in excellent agreement with 8D quantum dynamical results for the vibrational ground state, and the ν_1=1 symmetric and ν_3=1 asymmetric stretch states [118].

There are many problems with gauging the accuracy of QCT for gas phase reactions of polyatomic molecules like CHD_3 or CH_4 through comparison with experiments, and inferring the accuracy of QCT calculations for methane reacting on surfaces from these comparisons. One problem with gauging the accuracy of QCT through comparisons with gas phase experiments is that it is difficult for such experiments to measure absolute initial state-resolved integral cross sections for reaction. As a result, the comparison to experimental results for the initial state-resolved integral cross sections for reaction often requires normalization of the experimental data to the theory [42], or a comparison is made to ratios of cross sections for different initial states [119-120]. A second, and related problem is that molecular beam experiments on gas phase reactions often provide information at a high level of detail, such as product angular distributions, which are often also resolved with respect to the vibrational state(s) of the product(s) [121-123]. Even

though the QCT method has shown high accuracy also for some of these more detailed experiments [120], it would usually be expected to work best for more highly averaged quantities, such as initial state-resolved integral cross sections for reaction. A third problem is that comparisons of theory to experimental results can be complicated by issues like whether the entire rotational state population of the CD_3 fragment was probed in the experiment [124], and whether the calculations correctly treated the initial rotational (J,K) states of CHD_3 excited in the experiments to the ν_1=1 state [110, 124].

There have also been attempts to gauge the accuracy of QCT for gas phase reactions of CHD_3 or CH_4 through comparison with quantum dynamical calculations. The efforts we are aware of have typically employed reduced dimensionality Hamiltonians, i.e., a 7D Hamiltonian based on a model originally due to Palma and Clary [125] and an 8D Hamiltonian due to Liu et al. [126]. Results of the corresponding 7D calculations on Cl + CHD_3 [110, 119] or 8D calculations on O + CH_4 [42, 118] were then compared to full-dimensional QCT calculations on these systems, and also to experiment for Cl + CHD_3 [110]. On the whole, the quantum dynamical and QCT results were in quite good agreement with another for O as collision partner [42, 118], and the agreement was somewhat less good for the Cl atom [110, 119]. In the latter case, experiment could not yet be used to decide in favor of either method regarding the accuracy for the reaction of CH-stretch excited CHD_3, as theory and experiment did not address the same initial (*JK*) rotational state of CHD_3 [110], as should be necessary. In any case we argue that reduced dimensionality calculations cannot be used as the gold standard to test the quality of the full-dimensional QCT calculations. We argue that, for this, the approximations introduced in the quantum Hamiltonians are too severe. In particular, both the 7D and the 8D Hamiltonians assume that the non-reacting methyl fragment retains C_{3v} symmetry. While it is true in some sense that the Hamiltonian is representative of

both stretching and bending vibrations, the vibrations that break the symmetry of the remaining umbrella, such as the bending vibrations of CH_4, are not correctly described with these Hamiltonians. The accuracy of the reduced dimensionality approach has been argued on the basis of the good agreement obtained with full-dimensional quantum mechanical results for the H + CH_4 reaction[119]. However, this comparison concerned cumulative reaction probabilities, which are the micro-canonical equivalent of rate constants, and not initial-state resolved integral cross sections [127].

In summary, we argue that expectations concerning the accuracy of the QCT approach should be based on what is known concerning the accuracy of this approach for surface reactions. As outlined at the beginning of this Section, all existing knowledge suggests that the QCT approach should be accurate for the reaction of CH-stretch excited CHD_3 under the experimental conditions addressed here. The QCT method should also be accurate for at least a small energy window for laser-off reaction, where the incidence energy exceeds the zero-point energy corrected barrier height but the accuracy is not yet adversely affected by the contribution to the reactivity of CHD_3 states with excited CD-modes. As discussed above, the accuracy of QCT for these states is less certain.

3. Statistical Test Based on Stouffer's Z-score

A statistical test based on the Stouffer's Z-score [128] has been employed to also put the comparison of the theoretical and the experimental reaction probabilities on a statistical basis. Such tests are based on a null hypothesis that states that theory reproduces experiments, in which case one would expect that Stouffer's Z-score

$$Z_{comp} = \sqrt{\frac{1}{k}} \sum_{i=1}^{k} \frac{\left(P_i(AIMD) - P_i(\exp)\right)}{\sigma_i} \qquad \text{(S7)}$$

comes out with a close to zero value. In Eq.S7, k is the number of beam conditions for which a specific experiment (laser-off, or state-resolved) is performed, $P_i(AIMD)$ is the reaction probability computed with AIMD for the ith average collision energy, $P_i(exp)$ the corresponding experimental value, and σ_i the standard error in the difference. In the calculation of standard error in the difference of the reaction probabilities, the theoretical standard error was computed from $\sigma = \sqrt{p(1-p)/N_t}$, where p is the computed reaction probability ($P_i(AIMD)$), and N_t the number of AIMD trajectories used. The experimental error was evaluated from the differences between replicate measurements. In a test based on this statistic, first a required significance level is set that represents the probability of discarding the null hypothesis even though it is true (typically $\alpha = 0.05$, i.e., 5%). Then, the null hypothesis is rejected if the absolute value of the calculated test statistic differs from zero by more than the threshold value. This threshold or critical value is determined on the basis of k and the significance level α required. Stouffer's Z-score test is appropriate if theory and experiment shows similarly sized error bars, so that the one cannot be used as the "gold standard" to measure the quality of the other (if this were true, a chi-squared test[129] would be more appropriate).

4. The determination of the SRP density functional.

To determine the SRP functional, we first performed test calculations with the general purpose GGA functional PBE [64]. The laser-off reaction probabilities computed with this functional clearly overestimate the experimental laser-off reaction probabilities (see Fig.S6, noting that the PBE laser-off results might seem to agree well with experimental results, but these concern state-resolved reaction of ν_1=1 vibrationally excited CHD_3).

Based on very recent previous experience with CHD_3 + Pt(111) and with H_2-metal surface systems, we next switched to the use of vdW-DF correlation instead of PBE correlation (see Section 2.2). Test calculations for the C2 barrier geometry of Ref. [98] using various values of x in Eq.S5 and the energy shift between the computed PBE laser-off reaction probability curve and the experimental curve first suggested the use of $x = 0.75$. A limited set of AIMD calculations (using fewer trajectories per energy point than stated in Section 2.5) suggested that x should be reduced, and we next changed to a value of $x = 0.47$. Calculations with this x-value still underestimated the measured laser-off reaction probability (See Fig.S6). The energy shift between the curve computed with $x = 0.47$ and the experimental laser-off reaction probability curve, and reaction barrier heights computed for the previously mentioned barrier geometry using lower values of x, next suggested the use of $x = 0.32$. With this semi-empirically obtained value the experimental laser-off sticking probabilities are reproduced for the three lowest nozzle temperatures (550 - 650 K), for which CHD_3 is predominantly in its ground vibrational state, so that we expect the QCT method to work well. We call the functional with $x = 0.32$ the SRP32-vdW functional.

For $E_i > 125$ kJ/mol ($T_n \geq 700$ K) our calculations with the SRP density functional describe the the laser-off reactivity less well. This was already anticipated in the main paper and in Section 2.1, as for these T_n less than 60% of the CHD_3 molecules remain in their vibrational ground state, and there should be considerable population of CD-bend and CD-stretch excited states, while artificial surface induced quasi-resonant energy flow of vibrational energy between the CD bonds (artificial in the sense that quantization is broken) cannot be ruled out with the use of the quasi-classical trajectory method used within AIMD. As can be seen from Fig.1 of the main paper, the AIMD calculations overestimate the laser-off reactivity for $E_i > 125$ kJ/mol. We

speculate that this is due artificial flow of energy between the CD modes in CD-bend and CD-stretch excited molecules, which may lead to too much energy being present in one of the CD bonds, which would then artificially promote the reaction of these molecules through CD-bond breaking. Evidence that this mechanism might be responsible for the overestimation of the laser-off reactivity at high E_i comes from a plot of the fraction of CHD_3 molecules dissociating via C-H bond cleavage computed with AIMD for both laser-off and vibrational ground state reaction. For the two highest E_i, this ratio is well below 0.2 for the laser-off reaction (Fig.S7), suggesting CD bond breaking in excess of what is expected from a statistical point of view (0.25 for one CH bond vs. 3 CD bonds). This result would seem to be at odds with experimental results for CHD_3 + Ni(111), where the CH-bond breaking ratio is close to statistical for $T_n \geq 700$ K (see figure 2 of Ref.[3]). The results of Ref. [3] were obtained with He-seeding, and therefore for lower E_i, but there is no reason to assume that the results would become "less statistical" for similar T_n but higher E_i. While a statement has been made[116] in research on CH_4 + Ni(111) to the effect that "QCT vibrational efficacies are generally smaller than experimental values", this was done on the basis of reduced-dimensionality calculations employing a PES using a functional (PW91)[70] that tends to overestimate reactivity, which in general would be expected to lead to underestimated vibrational efficacies.

Figure S5 shows the interaction energy of a methane molecule with the ideal, static Ni(111) slab as a function of the distance between the center of mass of the molecule and the surface plane (Z coordinate) as calculated with the SRP32-vdW density functional. The geometry of the methane molecule has been kept fixed to its equilibrium gas-phase configuration. The top site, and an orientation of the molecule with one hydrogen atom pointing away from the surface (θ=0°) and the other three hydrogen atoms pointing towards the closest bridge sites have been

employed. However, very similar interaction energy curves are observed varying the impact site on the surface and the molecular orientation, especially at large distances ($Z \geq 4$ Å, not shown). An attractive physisorption well is observed with minimum at $Z \approx 3.5$ Å.

The interaction energy curve is compared to the curve computed with the same computational setup as used throughout this work but employing a much larger amount of vacuum space (30 Å instead of 13 Å). If this converged set-up is used, the molecule-surface interaction displays a well depth of approximately 20 kJ/mol (4.6 kcal/mol), which compares reasonably well with the approximate experimental value reported by Ceyer and co-workers (2.9 kcal/mol ≈ 12 kJ/mol [130-131]). Ceyer and co-workers used thermal desorption and observed zero-order desorption for coverages up to 0.09 ML, meaning that for these coverages there was not yet any clustering of methane molecules on the surface. Their value of the well depth was obtained assuming a pre-exponential factor of 10^{12} s^{-1} [130-131]. This assumption carries some uncertainty with it, which also leads to uncertainty regarding the actual value of the well depth that the experimentalists tried to measure.

It is therefore very encouraging that calculations with the opt-PBE-vdW-DF functional[74] reproduce the van der Waals well depth computed with SRP32-vdW to within 1.9 kJ/mol (1.7 kJ/mol) with the use of a vacuum length of 30 Å (13 Å, the most accurate result is obtained using 30 Å). This is encouraging because this functional shows chemical accuracy for the S22 database of van der Waals molecules, with a mean absolute deviation of only 1.45 kJ/mol from the reference well depth data (Ref.[74] and references therein). Taken together, these observations suggest that the SRP32-vdW-DF functional reproduces the well depth of CH_4 physisorbed on Ni(111) to within (or close to) chemical accuracy.

5. Consequences of different ways of extracting initial-state-selected reaction probabilities from experiments for the comparison with theory.

An estimate of $S_0^{v=0}$, which is unfortunately unknown directly from experiments, is necessary for determining $S_0^{v_1=1}$ (see Section 1.5 and Eq.S3). Here we discuss experimental values of $S_0^{v_1=1}$ obtained using three ways of estimating $S_0^{v=0}$, and we discuss their comparison to theory.

In the first method, which we have used in the paper, we have assumed that $S_0^{v=0}$ equals the experimental value of S_0^{off}, which is an upper limit on $S_0^{v=0}$. The results of using this method are shown in Fig.1 of the main paper. In the second method, $S_0^{v=0}$ has been calculated assuming that the ratio $S_0^{v=0}/S_0^{off}$ is the same for theory and experiment, by multiplying the ratio computed with AIMD with the experimental value of S_0^{off} to obtain an estimate of the experimental $S_0^{v=0}$. The $S_0^{v_1=1}$ values estimated in this way are shown in Figure S8. Finally, we have also simply used the theoretical values of $S_0^{v=0}$ together with the experimental values of S_0^{off} and of S_0^{on} to estimate $S_0^{v_1=1}$ values, and the results are shown in Figure S9. The deviations between the reaction probabilities estimated in these three ways are generally smaller than the error bars in the experimental values of $S_0^{v_1=1}$, which reflect the variance of replicate measurements of S_0^{off} and of S_0^{on}.

Altered experimental values of $S_0^{v_1=1}$ values affect the error analysis based on Stouffer's Z-score, and also the method in which we assess the accuracy of the theory by considering the horizontal distance (along the energy axis) of the computed sticking probabilities to reaction

probability curves fitted through the experimental data. The experimental reaction probabilities were fitted to a generalized logistic (LGS function, see also Fig.S10) [132]:

$$S(E_i) = A \Big/ \left[1 + \nu \exp\left(-\frac{(E_i - E_0)}{W}\right)\right]^{\frac{1}{\nu}} \quad \text{(S8)}.$$

Here, A is the maximum value of the reaction probability, W is related to the width (or, alternatively, the slope) of the reaction probability curve, the E_0 parameter defines its inflection point, and ν is a parameter describing the degree of asymmetry of the reaction probability curve [132]. The expression S8 has been shown [132] to yield better fits to experimental reaction probability curves than the often used symmetric S-shaped functions that are based on an error function or a tanh function, where the tanh based S-shaped function actually equals the LGS function in the limit ν=1 (see also Fig.S10) [132]. The fit coefficients obtained using Eq.S8 for the three different methods of computing the experimental value of $S_0^{\nu_1=1}$ from $S_0^{\nu=0}$ are presented in Table S5.

For the ν_1-excited simulations we calculate Stouffer's Z-score as 0.731 if method 1 is used to determine $S_0^{\nu=0}$ experimentally. This value is lower than the positive critical value associated with the two-sided test, meaning that the null hypothesis cannot be rejected at the stated significance level. The corresponding p-value is 0.47, meaning that if we would reject our null hypothesis the probability that we would do so even though this hypothesis should be correct is 47%. In other words, the deviations observed between the measured and calculated reaction probabilities do not represent statistical evidence that they should be different, and we may retain the hypothesis that the experiments are well described by the theory. On the other hand, for the laser-off simulations, we obtain a Stouffer's Z-score equal to 4.1, and we may reject the null hypothesis that the theory correctly describes laser-off reaction over the entire energy range investigated with a p-value of 4 x 10^{-5}. The large Z-score is due to deviations between theory and

experiment for high E_i, which were anticipated, for reasons discussed in the paper and above in Section 2.1. As discussed earlier, we only used the two laser-off data points with E_i = 112 and 121 kJ/mol for constructing the SRP density functional, but for the validation we used the v_1=1 data over the entire range of energies for which they were measured.

For the v_1-excited simulations we calculate a Stouffer's Z-score value of 1.45 if method 2 is used to determine $S_0^{v=0}$ from the laser-on and the laser-off measurements, and the theoretical ratio of $S_0^{v=0}/S_0^{off}$. This value is lower than the positive critical value for rejection of the null hypothesis, meaning that the null hypothesis cannot be rejected at the stated significance level. The corresponding p-value is 0.15, meaning that if we would reject our null hypothesis the probability that we would do so even though this hypothesis should be correct is 15%. Again, the deviations observed between the experimental and the theoretical state-resolved reaction are small, and we may retain the hypothesis that the experiments are well described by the theory. Regarding the other method to assess accuracy (on the basis of the horizontal distance of the computed points to the fit of the experimental data), the conclusions are improved w.r.t. method 1 for the four lowest energies, i.e., in all four cases the distances along the energy axis are smaller than 1 kcal/mol (≈ 4.2 kJ/mol). For the highest E_i we cannot calculate the distance to the fitted curve (22.5 kJ/mol), because the computed reaction probability exceeds the saturation value of the fitted reaction probability curve. However, this is a fitting problem, the calculated and experimentally determined reaction probability are in good agreement for this energy.

For the v_1-excited simulations we calculate a Stouffer's Z-score value of 0.54 if method 3 is used to simply set $S_0^{v=0}$ equal to its computed value. This value is again lower than the positive critical value, meaning that the null hypothesis cannot be rejected at the stated significance level. The corresponding p-value is 0.59, meaning that if we would reject our null hypothesis the

probability that we would do so even though this hypothesis should be correct is 59%. Again, the deviations observed between the computed and measured state-resolved reaction probabilities do not present statistical evidence that they should be different, and we may retain the hypothesis that the experiments are well described by the theory. Regarding the other method to assess accuracy (on the basis of the horizontal distance of the computed points to the fit of the experimental data), the conclusions are unchanged w.r.t. method 1. In four cases the distances along the energy axis are smaller than 1 kcal/mol (≈ 4.2 kJ/mol), in one case the distance is slightly larger (for the highest E_i, see Fig.S9), which we attribute to statistical error. We conclude that using different methods (methods 2 and 3) to obtain the v_1=1 reaction probabilities from the experimental data (and, in part, from theory) does not change the conclusions regarding the accuracy of the theory for these reaction probabilities that we arrived at with method 1, which were discussed in the paper.

6. Extracted minimum barrier height and PES information; verifying accuracy.

The barrier heights with and without zero-point energy (ZPE) corrections (the latter assuming CH bond dissociation, and reporting the result for both CH_4 and CHD_3) using the SRP32-vdW functional and the CI-NEB method are presented in Table S6. The numbers in Table S6 have been corrected for the finite interaction the molecule still has with the slab through a comparison with calculations in which a vacuum length of 30 Å was used rather than of 13 Å.

Our minimum E_b value (97.9 kJ/mol) differs by only 8 kJ/mol from the value (89.7 kJ/mol) that was determined [133] through a mostly experimental procedure that only requires the vibrational zero-point energy at the barrier as a theoretical input, but requires an assumption about the efficacy of the vibration excited experimentally for promoting reaction [133]. In this procedure [133], the effect of averaging over incidence energy present in the molecular beam was

deconvoluted in an approximate way. For a low enough surface temperature, the procedure gave a kink in the experimental reaction probability as a function of incidence energy, when the measurement was done in an initial vibrational state resolved manner (the ν_3 asymmetric stretch state of methane was excited with one quantum). This kink was interpreted as a state-resolved reaction threshold, which was evaluated as 42 kJ/mol for ν_3 v=1 CH_4 + Ni(111) [133]. Next, the assumption was made that the added vibrational energy (36 kJ/mol for the ν_3 mode) is completely used to surmount the barrier near the threshold. Addition of these energies can provide an estimate of the activation energy for CH_4 in its ground vibrational state, which can be interpreted as the zero-point corrected barrier height. If we use our computed zero-point energy for CH_4 + Ni(111) at the transition state (11.7 kJ/mole, from the data for the C2 geometry in Table S6) to obtain the barrier height estimated in this way, we obtain the value of 89.7 kJ/mol. The comparison suggests the value obtained with the mostly experimental procedure to be remarkably accurate, as the difference with our semi-empirical value, which should be the most accurate, is only 8 kJ/mol.

The value obtained with the above procedure but using the PBE zero-point energy correction at the barrier (quoted as 15.1 kJ/mol in Ref.[133]) yields a somewhat higher (by 3.4 kJ/mol) value of the "experimental" barrier height, i.e., 93.1 kJ/mol, differing from our present semi-empirical value of 97.9 kJ/mol by only 4.8 kJ/mol, and in good agreement with the barrier height obtained with the PBE functional, of 96.9 kJ/mol (the difference being only 3.8 kJ/mol). While this might suggest that the PBE functional describes the reactivity of methane on Ni(111) as accurately as the functional determined semi-empirically here, we note that AIMD calculations performed by us in a preliminary phase of this project considerably overestimated the measured laser-off reaction probabilities at low incidence energies (see Fig.S6), as previously observed for CHD_3 +

Pt(111) [23]. This confirms recent findings [134] that the reaction probability curve does not only depend on the minimum reaction barrier height, but also on the shape of the potential energy surface, which, for the PBE functional, would, for instance, not exhibit a van der Waals well.

The plot of idealized reaction probabilities described by Eq. S8 (i.e., Fig.S10) may also be used to explain which information about the distribution of barrier heights can be recovered from measured and computed reaction probability curves. Here, we closely follow arguments presented earlier in Ref.[132] and the Supporting Material to Ref. [27].

According to a classical version of the hole model [135], the sticking probability can be calculated according to

$$S\left(E_i\right) = \int_0^{E_i} N(E')dE' \qquad \text{(S9)}$$

where *N(E)* is the fractional number of barriers with an energy between E and E + dE. For CHD_3 reacting on any metal surface, N(E) would be evaluated by considering all coordinates orthogonal to the dissociating CH stretch coordinate and the molecule-surface distance Z, and computing the barrier height for dissociation in this reduced two-dimensional space for each volume element in the space orthogonal to it [27, 135] (note that there is no need of invoking a harmonic expansion around the minimum barrier geometry for computing this barrier, as done in the original version of the hole model [135]). If *N(E)* is assumed to be a Gaussian function, the resulting sticking probability curve can be described in terms of an expression including an error function

$$S(E) = \frac{A}{2}\left[1 + erf\left(\frac{E - E_0}{W}\right)\right] \qquad \text{(S10)}$$

as discussed by Luntz in the framework of a dynamical model for CH_4 + Ni(100). Here, *A* is the maximum value (or saturation) value of the reaction probability, *W* is a width parameter

describing the steepness of the curve, and E_0 the energy at which the reaction probability becomes equal to half its maximum value (see also Fig.S10).

While the classical hole model often yields a quite reasonable approximation to the sticking probability curve computed with a sophisticated dynamics method for an activated reaction, as previously demonstrated for H_2 + Cu(110) [136], in practice deviations will occur through dynamical effects. Assuming that these are well described by the dynamics method used (and they should be for our problem with the QCT method used for the regime of experimental conditions addressed, see Section 2.6), the following will still be true in an approximate sense. First, if a calculated state-selected reaction probability curve is in quantitative agreement with the experimental reaction probability curve, the underlying model for the molecule-surface interaction should accurately describe *N(E)*. For a diatomic molecule like H_2 reacting on a metal surface, this is usually taken to mean that the potential model accurately describes how the barrier height depends on the impact site (X,Y) on the surface (corrugation of the barrier height) and on the orientation of the molecule with respect to the surface, which is, for a diatomic molecule, specified by the polar angle θ and the azimuthal angle ϕ (anisotropy of the barrier height). This can be generalized to polyatomic molecules like CHD_3 by now specifying the orientation in terms of three angles (the Euler angles of orientation), and by also taking into account that surface atom vibrations may modify the barrier height [25, 100]. We have used this line of reasoning to argue in the main paper that the close agreement between theory and experiment for the state-selected reaction probability curve implies that the SRP32-vdW functional accurately describes how the barrier height varies with impact site and orientation of the molecule.

Second, if the computed reaction probability curve also closely (within chemical accuracy) follows the experimental curve near the reaction threshold for laser-off reaction (which we essentially see for average incidence energies between 101 and 121 kJ/mol, where the laser-off reaction probability is just above 1% and where the molecule is predominantly in its ground vibrational state), the potential model can be expected to yield a chemically accurate value of the minimum reaction barrier height. For this reason we argue that the minimum barrier height extracted with the CINEB-method using the SRP32-vdW functional for the static, ideal Ni(111) surface should be of chemical accuracy, and of use for benchmarking purposes [137], as previously argued for H_2 + Cu(111) [27]. Note that the laser-off point for the lowest E_i (101 kJ/mol) was not initially used to derive the SRP functional and determine the minimum barrier height, but measured and computed later for additional validation, and to increase the confidence in our procedure to determine the reaction barrier height.

Finally, and not strictly related to the hole model argument, we can use the comparison between theory and experiment to obtain information concerning the barrier geometry. The calculations reproduce the experiments for the so-called vibrational efficacy, which measures how efficiently vibrational excitation (in this case, of the CH-stretch mode) promotes the reaction. For this purpose, we can use the laser-off experiments for the lowest incidence energies, where most molecules are in their vibrational ground state, and the results for $S_0^{v_1=1}$ for the same incidence energies. Theory reproduces experiments for both cases. Polanyi's rules [138], which relate the vibrational efficacy to the location of the barrier height in the coordinate corresponding to the dissociation bond, then suggest that the SRP32-vdW functional also accurately describes the barrier geometry.

Arguments along the lines presented above can also be used to evaluate the extent to which theory and experiment are in quantitative agreement for other dissociative chemisorption problems. To start with an example from our own work [40], for H_2 + Ru(0001) experimental sticking probabilities could not be reproduced using an exchange functional of the form of Eq.S5 in combination with the standard PBE correlation functional. This gave a reaction probability curve that intersected the experimental sticking probability curve, but was too steep to follow it over the range of energies for which experimental sticking probabilities were available (see Fig.15B of Ref.[68]). This behavior could only be corrected by combining Eq.S5 for exchange with vdW-DF correlation [72]. This yielded a reaction probability curve with correct values for the reaction threshold and the width *W* of the reaction probability curve, suggesting that the corrugation and the anisotropy of the barrier height are only correctly described using vdW-DF correlation for H_2 + Ru(0001) [40].

Secondly, an accurate [38] or reasonably accurate [23] description of the state-specific reaction probability for one specific initial excited vibrational state over a wide range of energies is, taken by it self, no guarantee that the molecule-surface interaction model will allow the accurate description of the minimum barrier height for the system under investigation. In the examples referenced above [23, 38], QCT calculations achieved good agreement with experiments on dissociative chemisorption of ν_3=1 CH_4 on Pt(111) [38], and AIMD calculations reasonably good agreement with experiments on dissociative chemisorption of ν_1=1 CHD_3 on Pt(111) [23] using an underlying PBE molecule-surface interaction model. However, this agreement was based on cancellation of errors between a too low vibrational efficacy and a too low barrier height, as the laser-off reaction probability was overestimated with PBE [38].

It should also be stressed that it should only be possible to extract reliable information from a potential model if the dynamics model used to perform the calculation of the reaction probability is accurate, so that no cancellation occurs between errors arising from the dynamical model and the potential model (the functional used). For instance, we would not expect [23, 139] to be able to extract chemically accurate information regarding the molecule-surface interaction from calculations that make the rotationally adiabatic approximation to model the rotations of the molecule, even though such calculations might provide highly useful mechanistic insights regarding the differing promoting effects of exciting specific initial vibrational modes on reaction [34, 140] (see also Figure 3 and its discussion below in Section 7).

7. Additional AIMD results on the dynamics of reaction and scattering.

The AIMD calculations yield interesting insights concerning where on the surface the molecules react, and at which orientations. Figure S11 illustrates in another manner than Figs.3A and 3B that, for a similar value of S_0 (*i.e.*, 0.03), reaction on Ni(111) occurs at a wide range of impact sites, whereas CHD_3 reacts only near on-top sites in the very similar methane + Pt(111) system. Figure S12 shows that at E_i higher than the energy considered in Fig.3 of the main paper the molecules react even further away from the minimum barrier top sites. As discussed in the main paper, this has consequences for which approximations are applicable to the rotations in quantum dynamics approaches. Figure S13 shows that on approach to the surface, for the normal incidence conditions simulated, the molecules hardly travel along the surface: the lateral distance between the impact point aimed at initially and the impact point at the point of reaction or scattering is quite small, the distribution of this lateral distance peaking below 0.1 Å. As discussed in the main paper, this suggests that sudden approximations to the motion parallel to

the surface should work quite well in quantum dynamics. In such approaches, one computes the reaction probability for a range of impact points (X,Y), after which the overall reaction probability is computed by averaging over the reaction probabilities computed for the (X,Y) impact points considered [140].

Concerning the rotational dynamics, our results for Ni(111) (Figs. 3C and S14) confirm earlier findings for Pt(111) [23, 139] that the rotations cannot be treated within the often made [140] rotationally adiabatic approximation, and this holds true even for the highest E_i (Fig.S14). This approximation assumes that the molecule, while interacting with the surface, stays in its rotational ground state while travelling from the gas phase to the barrier. This would only hold true in an approximate sense if the initial β distribution of the reacting molecules should be close to the random initial distribution in Figs. 3C and S14 (β is the angle between the CD_3 umbrella axis and the surface normal, and θ is the angle between the reactive CH bond and the surface normal, see Fig.2). Then, there would be near to perfect steering of the molecules to their preferred reactive orientation at the point where reaction occurs. Figs. 3C and S14 show that this not the case for reaction on Ni(111), with the initial β distribution clearly differing from the initial random distribution (which is according to $\sin\beta$, for J=0).

The AIMD calculations also show that the β angle between the umbrella axis of a reacting molecule and the surface normal (Fig.2) undergoes a considerable change during its approach to the barrier for all E_i investigated (Figs.3C and S14). This suggests that the rotational sudden approximation for the associated tumbling rotation should be inaccurate, as also found very recently for CHD_3 + Pt(111) [139]. Sudden approximations to the θ angle between the reacting C-H bond and the surface normal (see Fig.2) should also not work well: There is not only a focusing in θ, but on the whole the distribution of θ shifts towards a smaller value for all E_i investigated

(Fig.3C), which was not seen in earlier calculations for Pt(111) [23]. This also holds for the highest E_i, where sudden approximations would be assumed to work best (Fig.S14).

8. The accuracy of approaches using only semi-local exchange to computing dissociative chemisorption barriers for molecules on transition metals

It is not obvious that SRP functionals containing semi-local exchange, as in Eq.1, should be capable of describing the dissociative chemisorption on molecules on metal surfaces. Specifically, DFT studies have shown that GGA functionals like the PBE and the RPBE functional both systematically underestimate barriers for gas phase reactions. For instance, in the description of gas phase reaction barriers in the so-called DBH24/08 database [141], which contains examples of H-atom and heavy atom (i.e., heavier than He) transfer reactions, nucleophilic substitution reactions, and uni-molecular and association reactions, the mean signed error (MSE) is actually equal to minus the mean unsigned error (MUE) for the PBE (MSE = -8.2 kcal/mol) [142] and RPBE (MSE = -6.3 kcal/mol) [142] functionals. In other words, if this performance should carry over to dissociative chemisorption reactions on late transition metals, the performance of SRP functionals as given by Eq.1 and similar expressions featuring GGA correlation [27, 67] should not be better than that of the RPBE functional, and it should not be good. Fortunately, we know from research on ammonia production (which should mostly reflect dissociative chemisorption of N_2 on defected Ru surfaces as rate limiting step) [71] and on dissociative chemisorption of H_2 + Cu(111) [27, 67], H_2 + Cu(100) [28], H_2 + Ru(0001) [40, 68], H_2O + Ni(111) [33], CH_4 and Pt(111) [47], and now also CH_4 + Ni(111) (this work) that it is possible to bracket the barrier height with functionals exhibiting GGA [27-28, 33, 47, 68, 71] or vdW-DF [40, 47] correlation, and using PBE exchange at

the one and RPBE exchange at the other extreme. This is important as adding exact exchange, which allows a more accurate description of gas phase reaction barrier heights [63, 142], would make the SRP-DFT-AIMD calculations much more expensive (the computational cost of DFT with hybrid functionals scales as N^4, where N is the number of electronic basis functions, with the GGA the scaling is as N^3 [141]). The alternative of increasing the exchange enhancement factor beyond that of the RPBE functional should seriously deteriorate the description of the metal [143].

An explanation often invoked for the poor performance of ordinary GGA functionals for gas phase reaction barrier heights (i.e., the underestimation of the transition state energy relative to the energy of the reactants) is that these functionals underestimate energies in situations where bonding electrons are allowed to delocalize over additional nuclei [144-146]. Provided that the underlying ideas are correct, the explanation of the observed good performance of GGA functionals for dissociative chemisorption on late transition metals may then be phrased as follows. First, in the transition state the initially localized electrons that form the breaking molecular bond will delocalize towards metal centers, and this should over-stabilize the transition state. Second, two electrons coming from the metal, which will initially be delocalized over the metal surface, have to become more localized in the formation of the emerging bonds between the metal and the molecular fragments, which will destabilize the transition state. In view of the observations of good GGA performance for dissociative chemisorption on transition metals, these opposing effects apparently cancel, and allow one to bracket the barrier height with less repulsive PBE exchange on the one hand, and more repulsive RPBE exchange on the other hand. Here, as far as the bracketing is concerned it should not really matter whether GGA correlation [64] or vdW-DF [72] correlation is used, this distinction only becomes important when it comes to reproducing the shape of the reaction probability curve (i.e., its slope or width) in

addition to the reaction threshold [40, 137]. Here, it is probably also important that late transition metals have high work functions [50] and molecules like H_2, CH_4, and H_2O have negative electron affinities, so that there is no large partial charge transfer from the surface to the dissociating molecule in the transition state. The reason is that the concept of "delocalization" is connected with the concept of "fractional charge" [144-147], i.e., the LDA and gradient corrected functionals fail for effective charges of the nuclei significantly differing from integer numbers.

The above observations and explanation are important to the present applicability of the SRP-DFT-AIMD approach to dissociative chemisorption on late transition metals, which is of obvious relevance to heterogeneous catalysis. For this, we first note that one can also use the SRP-DFT approach with functionals incorporating exact exchange, and varying the amount of exact exchange is actually the way in which SRP-DFT was first applied in applications to chemistry in the condensed phase [26]. Janesko et al. have recently used such an approach to study whether it is possible to obtain a simultaneously accurate description of the adsorption energy and diffusion barrier of atomic oxygen on graphene [148]. In a recent article [149], it has been argued that the "GGAs' underestimate of gas-phase reaction barriers carries over to reactions on surfaces". As we will argue below, we think that this statement is too general, and that it is necessary to distinguish between dissociation reactions on late transition metals on the one hand, and dissociation reactions on semi-conductor surfaces and on (simple) metals with possibly substantial accompanying charge transfer on the other hand. When dealing with dissociative chemisorption reactions on late transition metals, and perhaps also in many cases for such reactions on simple metals, it should be possible to implement SRP-DFT-AIMD using the computationally tractable version used here, which only incorporates semi-local exchange.

Many examples given in Ref. [149] of surface reactions for which the use of semi-local exchange leads to underestimated barriers concern reactions on semi-conductor surfaces, and in these cases we do not expect the cancellation effect referred to above to occur. In these cases the use of an SRP functional with exact exchange added, as advocated in Ref. [149], may well be appropriate. The only examples provided in Ref. [149] where the RPBE functional might seem to underestimate the reaction barrier height for dissociative chemisorption on a metal concern O_2 + Al(111) [150-151] and H_2 + Mg(0001) [152]. In the former case, one explanation holds that DFT at the GGA level breaks down because it cannot describe the substantial charge transfer that occurs in the transition state from Al(111) to the O_2 molecule [153]. This would break the balance due to the fractional charge effect discussed above. Several groups have shown that this can be remedied by the fix of adding exact exchange to describe this particular case [154-156], as also noted in Ref.[149]. Note, however, that an alternative explanation holds that the apparent presence of a substantial barrier observed experimentally for O_2 on Al(111) is due to spin-selection rules, and that the reaction may be described rather accurately with a GGA functional in an non-adiabatic approach [150].

For H_2 + Mg(0001) it has been argued that DFT using the RPBE functional should underestimate the barrier height, because the use of quantum Monte Carlo leads to a higher barrier height than obtained with RPBE, by 10.6 kJ/mol [152]. We argue that this result does not necessarily point to RPBE underestimating the experimental barrier height for H_2 + Mg(0001). First of all, while accurate in principle, we do not yet know how accurate quantum Monte Carlo may be in practice for reaction barriers of molecules dissociating on metals. The reason is quite simple: experimental information on such dissociation barriers is for most systems either absent, or highly inaccurate, as is the case for H_2 + Mg(0001) [152]. Secondly, the DFT-RPBE result for the

barrier (103 kJ/mol) actually overestimates the experimental barrier height estimated by Pozzo and Alfé (96 ± 14 kJ/mol), which seems to have been overlooked in Ref.[149]. Finally, even if DFT-RPBE would underestimate the barrier height for H_2 + Mg(0001), this could in part be due to charge transfer from the metal to the molecule in the transition state, as the work function of Mg(0001) is rather low (3.84 eV or 370 kJ/mol) [157]. If this would hold true, it might indeed be necessary to use an SRP density functional with adjustable exchange in it. However, we regard these two examples as (possible) exceptions to a more general rule that SRP-DFT using semi-local exchange should generally be applicable to dissociative chemisorption on metal surfaces, and that this rule should certainly hold for molecules dissociating on transition metal surfaces in the absence of substantial charge transfer. This should serve to make SRP-DFT-AIMD applicable in a computationally tractable framework to a wide range of cases relevant to heterogeneous catalysis with present-day computational facilities.

Supporting Tables.

Table S1. Parameters employed to simulate the CHD_3 molecular beams in the present work (using H_2 as seeding gas), and parameters characterizing the beams used in Ref.3 (with He seeding). For the latter, which we report for benchmarking purposes, we give the average incidence energy E_i here, whereas in Table 1 of Ref.3 the incidence energy associated with the stream velocity was reported. For T_n = 600 K we give parameters describing two experiments of Ref.3 here, which were pooled as similar reaction probabilities were obtained in Ref.3 for these beams. The He seeded beams had 1.5% of CHD3 in them. Parameters for the 600, 700, and 830 K nozzle beams are from time of flight measurements. Values of v_0 and α for the 550K and 900K He-seeded beams were estimated from the observed linear dependence of E_i and α^2 on T_n.

Nozzle temperature, T_n (K)	$\langle E_i \rangle$, kJ/mol	Stream velocity, v_0 (m/s)	Width parameter, α (m/s)	Seeding gas
550	101.1	3240.00	174.31	H_2
600	112.3	3418.09	168.02	H_2
650	121.2	3547.60	191.51	H_2
700	130.7	3683.31	205.42	H_2
750	136.4	3760.72	216.91	H_2
900	160.4	4070.12	274.51	H_2
550	53.4	2355	122.3	He
600	57.0	2433	137.2	He
600	58.8	2468	145.9	He
700	68.4	2657	181.9	He
830	79.7	2870	191.3	He
900	87.9	3012	205	He

Table S2. Effect of intrapolyad cooling on computed sticking probabilities. Laser-off sticking probabilities computed assuming a simple Boltzman distribution of vibrational states (S_0), their associated error bars, the contribution to the sticking probability from the N = 0 - 4 polyads using simple Boltzman weighting (S_0(P0-4) Boltzman), and the contribution to the sticking probability from the N = 0 - 4 polyads obtained after reweighting the sticking trajectories taking intrapolyad cooling into account ((S_0(P0-4) reweighted). No attempt was undertaken to reweight states in polyads with N > 4, as these polyads merge (their energies start to overlap); the total weight of these states is given as population (P>4). On average, taking polyad intracooling into account leads to slightly smaller laser-off sticking probabilities.

T_N (K)	E_i (kJ/mol)	S_0	Error bars (+/-)	Population (P>4)	S_0 (P0-4) Boltzmann	S_0 (P0-4) reweighted
550	101.1	0.014	0.004/0.003	< 0.001	0.014	0.012
600	112.3	0.028	0.006/0.005	0.001	0.027	0.027
650	121.2	0.040	0.007/0.006	0.001	0.039	0.040
700	130.7	0.108	0.010/0.009	0.003	0.107	0.098
750	136.4	0.124	0.015/0.014	0.006	0.122	0.123
900	160.4	0.280	0.021/0.020	0.026	0.262	0.255

Table S3. Parameters used to predict f_{exc} for beams used in this study. Sections 1.3.2, 1.3.3, and 1.5.3 describe the calculations leading to estimates of $f_{v=0}$, the fraction of molecules in the vibrational ground state, estimates of the rotational temperature of the beam, T_{rot}, and f_{rot}, the fraction of molecules in the J"=1, K"=0 level from which infrared excitation occurs. The total fraction of CHD_3 molecules in the beam excited to the ν_1 v'=1, J'=2, K'=0 state, f_{exc} is calculated from these quantities using Eq. S4.

T_n, K	$f_{v=0}$	T_{rot}, K	f_{rot}	f_{exc}
300	0.974	7.4	0.219	0.107
600	0.686	14.8	0.163	0.0559
650	0.624	16.0	0.153	0.0477
700	0.566	17.3	0.144	0.0408
750	0.508	18.5	0.135	0.0343
900	0.362	22.2	0.113	0.0205

Table S4. Convergence tests for the energy barrier (E_b, in kJ/mol) for CH_4 + Ni(111). The C2 transition state geometry from Refs. [98-99] has been employed, together with the PBE density functional. The value of E_b has been calculated varying the supercell size, the number of atomic layers in the slab, the k-point grid mash and the cutoff energy (in eV, 1 eV ≈ 96.485 kJ/mol) for the plane wave expansion. The employed computational setup has been highlighted. We also add reaction barrier heights computed with the PBE and PW91 functionals in other studies, which have used slightly different geometries.

Functional	Supercell	# Layers	k-point grid	Cutoff energy	E_b
PBE	2x2	4	8x8x1	350	100.8
PBE	2x2	4	8x8x1	400	101.2
PBE	2x2	4	8x8x1	500	101.2
PBE	2x2	4	8x8x1	650	101.4
PBE	2x2	4	16x16x1	400	100.5
PBE	2x2	6	8x8x1	400	102.1
PBE	2x2	8	8x8x1	400	100.9
PBE	**3x3**	**4**	**4x4x1**	**350**	**94.9**
PBE	3x3	4	4x4x1	400	95.4
PBE	3x3	4	6x6x1	400	95.6
PBE	3x3	6	6x6x1	400	95.7
PBE	4x4	4	4x4x1	400	95.2
PBE	4x4	6	4x4x1	400	94.9
PBE	2x2	4	8x8x1	400	102.8 [98]
PBE	3x3	4	8x8x1	400	97.0 [36]
PW91	2x2	4	8x8x1	375	105.5 [100]
PW91	3x3	4	8x8x1	375	98.2 [100]
PW91	4x4	4	8x8x1	375	96.4 [100]
PW91	2x2	5	16x16x1	375	104.6 [100]
PW91	2x2	3	3x3x1	350	105.2 [31]
PW91	2x2	3	9x9x1	400	105.4 [101]

Table S5. Numerical parameters of fits to experimental reaction probability curves using Eq. S8.

Method	method 1		method 2		method 3	
	S_0^{off}	$S_0^{v_1=1}$	S_0^{off}	$S_0^{v_1=1}$	S_0^{off}	$S_0^{v_1=1}$
A	0.380	1.000	0.380	0.379	0.380	0.600
E_0 (kJ/mol)	152.7	159.6	152.7	120.5	152.7	139.3
W (kJ/mol)	25.5	34.2	25.5	23.2	25.5	19.2
ν	0.407	0.437	0.407	0.000	0.407	0.742

Table S6. Transition state (TS) energies (E_b) and zero-point energy corrected transition state energies for CH-bond breaking in CH_4 and CHD_3 (E_b^c) as result of CI-NEB calculations. The TS energies accounting for ZPE correction are also reported. The SRP32-vdW functional has been employed here. The numbers in Table S2 have been corrected for the finite interaction the molecule still has with the slab through a comparison with calculations in which a vacuum length of 30 Å was used. For the meaning of the coordinates, see Fig.2 in the main paper. For the notation used for the impact site (close to the top site) and approximate molecular orientation characterizing the transition state, see Ref. [98].

TS Geometry	Z_C (Å)	r_{CH} (Å)	θ (deg)	β (deg)	E_b (kJ/mol)	E_b^c , CH_4 (kJ/mol)	(E_b^c), CD_3-H (kJ/mol)
B1	2.169	1.638	134.6	165.6	99.5	87.1	86.3
B2	2.175	1.612	135.6	164.8	98.7	86.8	85.9
C1	2.171	1.632	134.7	165.7	98.8	86.5	85.7
C2	2.176	1.606	135.7	164.7	97.9	86.2	85.3

Supporting figures.

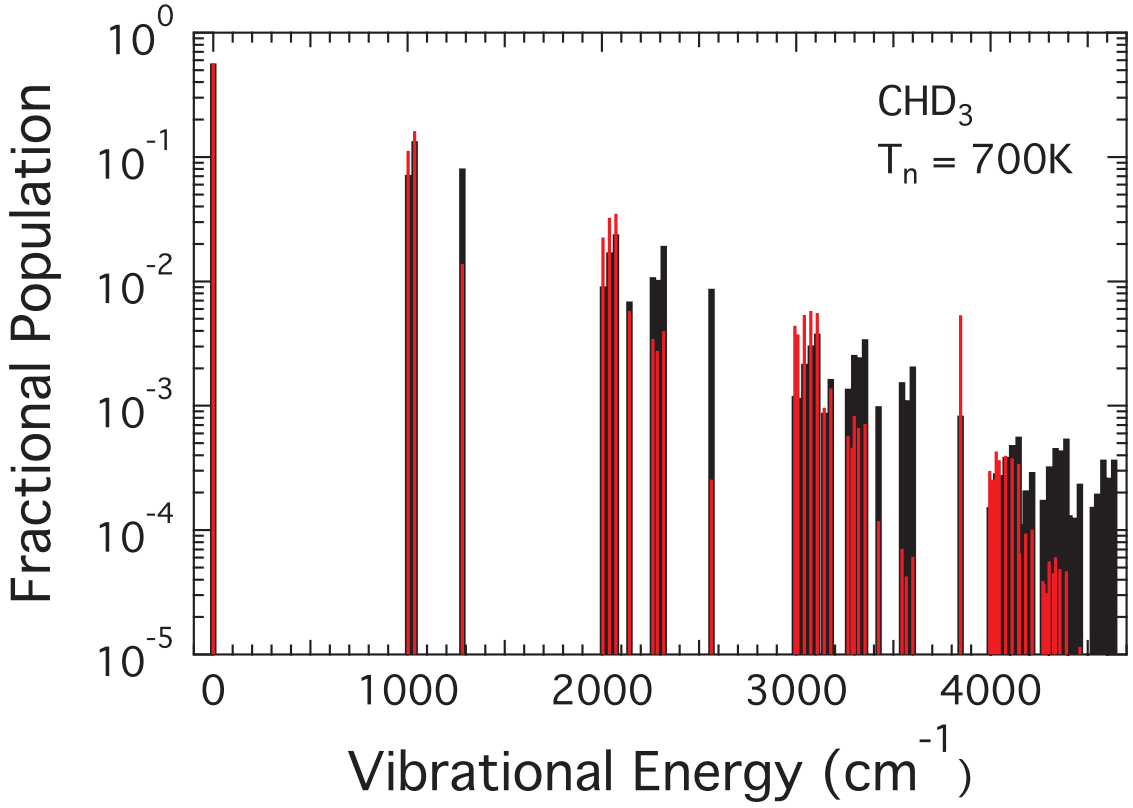

Figure S1. Calculated fractional populations for the vibrational states of CHD_3 at T_n = 700K. Black bars show the Boltmann distribution at 700K, while red bars show populations that result from intrapolyad cooling. The relative integrated population of the polyads is fixed at the value for a 700K Boltzmann distribution, while the relative populations of individual states within each polyad is calculated for a polyad temperature of 144K.

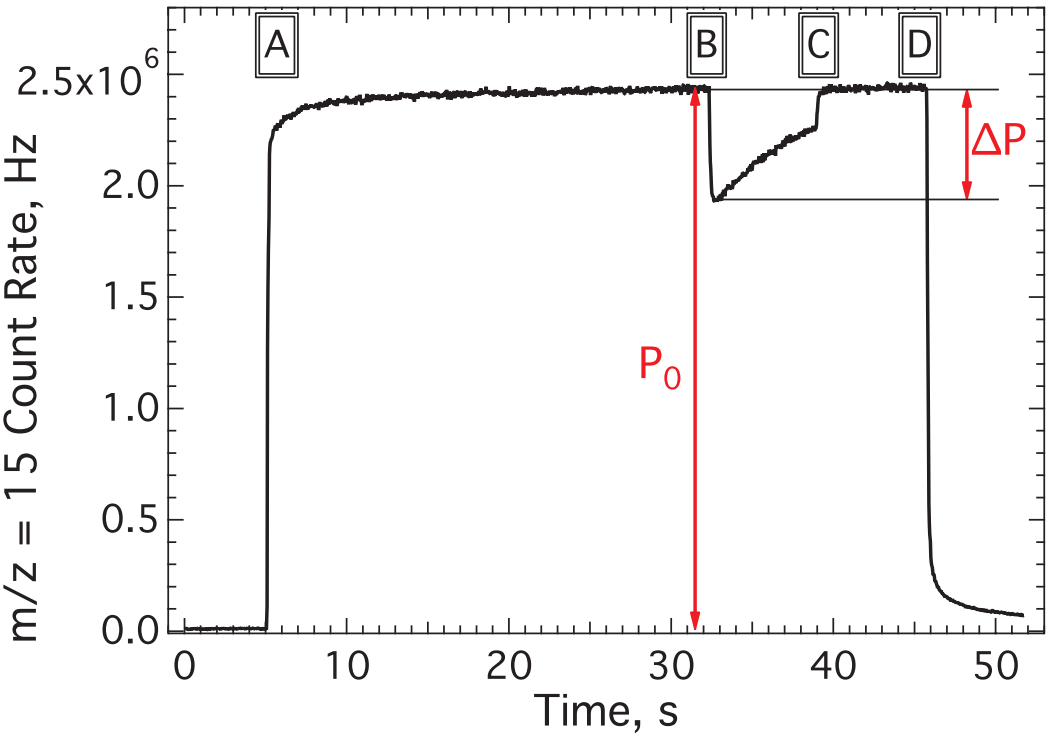

Figure S2. Molecular beam reflectivity measurement of a laser-on, T_n = 900K beam impinging on a 550K Ni(111) surface. The beam was introduced into the UHV chamber at t=5 sec and the gold flag removed from in front of the surface at t=32 s. The flag was inserted back into the beam path at t=38 sec, and the beam was blocked from entering the chamber at t=46 sec.

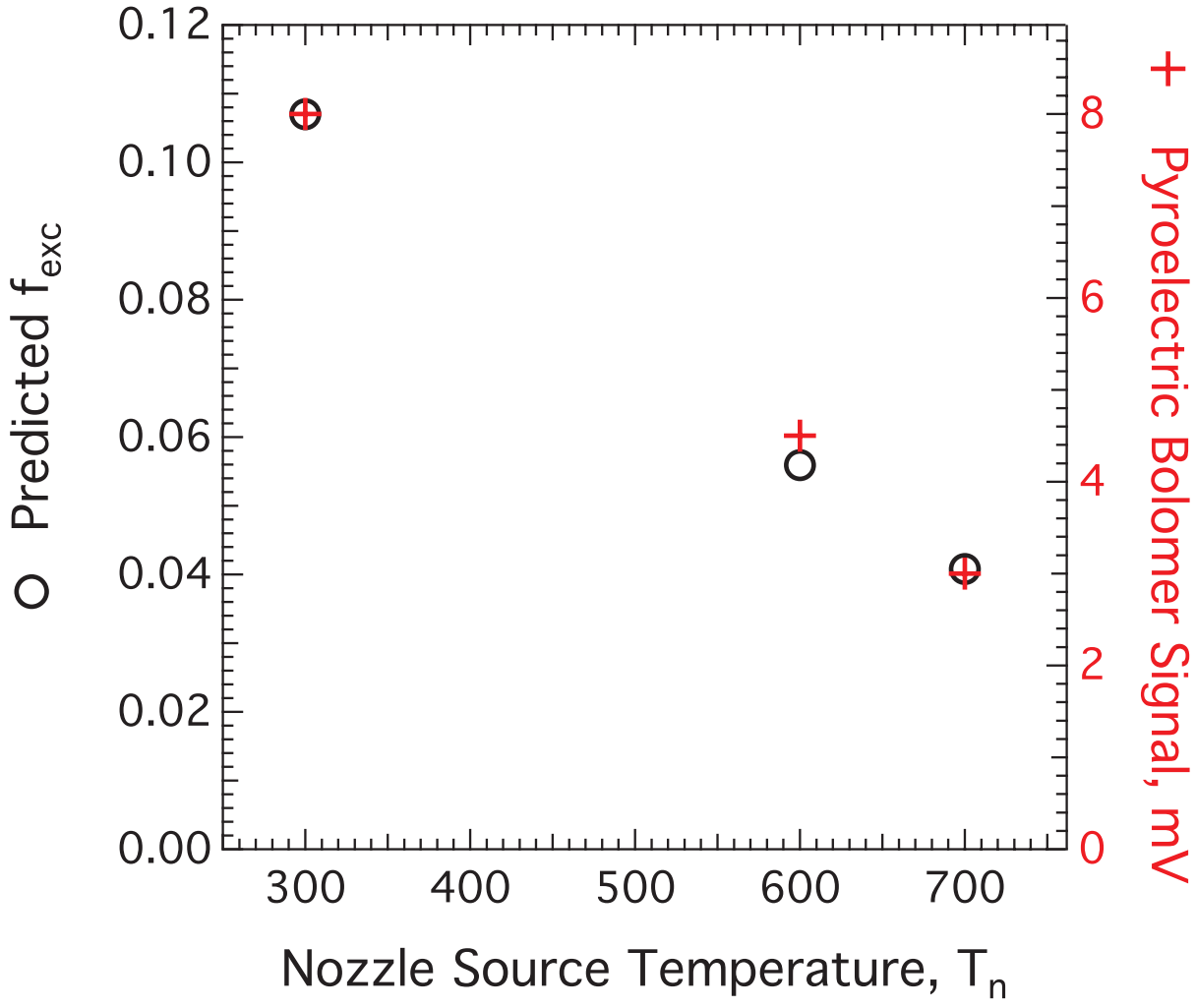

Figure S3. Comparison of predicted f_{exc} based on estimates of the rotational and vibrational temperature of the beam (black circles) and the pyroelectric bolometer signal measured at each of three nozzle source temperatures. The bolometer signal was constrained to correspond to the predicted f_{exc} at 300K, where rotational and vibrational cooling is nearly complete and well defined.

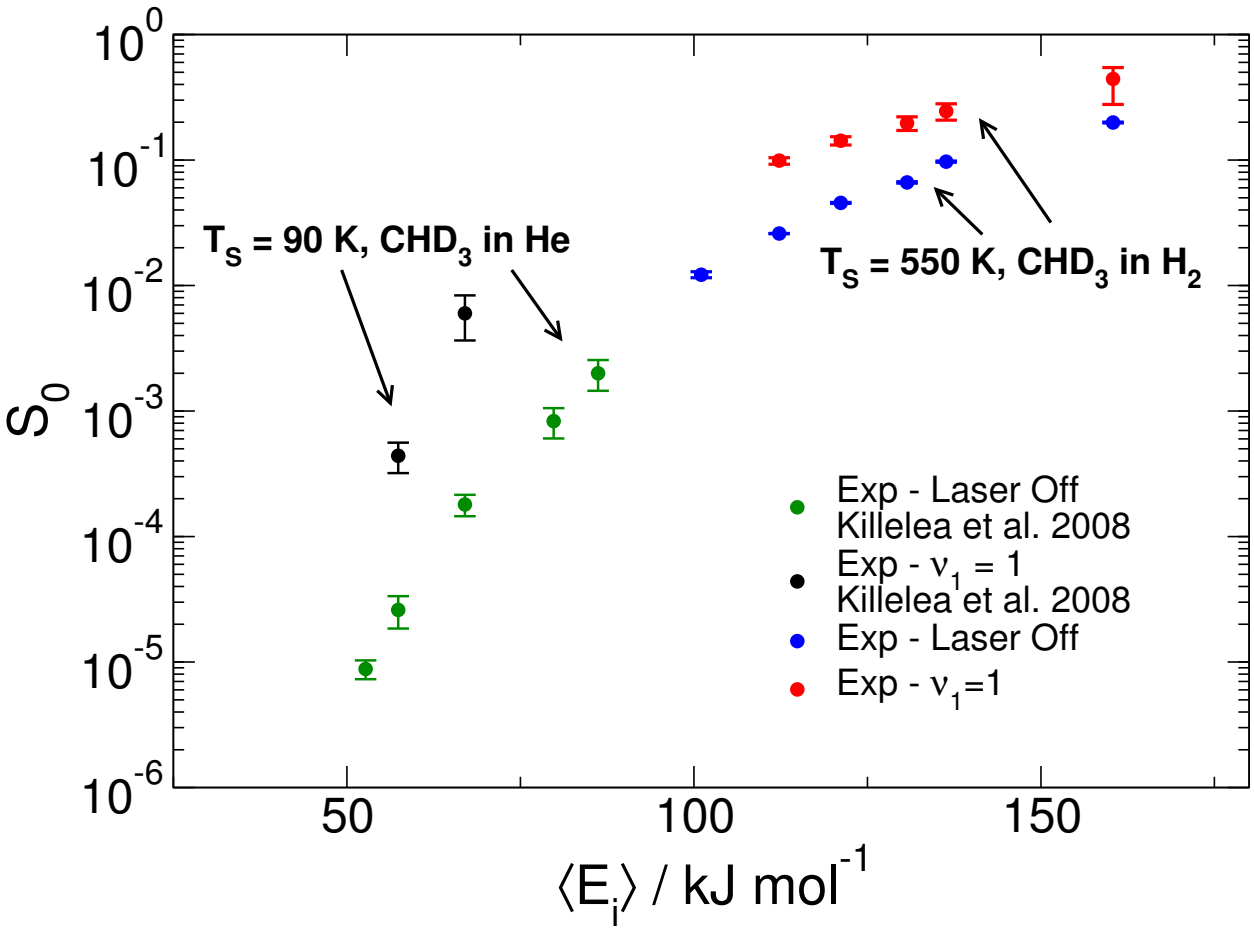

Figure S4. Two sets of measured sticking probabilities are shown for both laser-off reaction and reaction of CHD_3 (ν_1=1). The results of Ref.[3] for $E_i \leq 95$ kJ/mol were obtained using He as seeding gas and using T_s = 90 K and T_n values in the range 550 to 900 K (green circles for laser-off reaction, black circles for CHD_3 (ν_1=1) reaction). The results obtained in the present work for $E_i \geq 100$ kJ/mol were obtained using H_2 as seeding gas and using T_s = 550 K and T_n values in the range 550 to 900 K (blue circles for laser-off reaction, red circles for CHD_3 (ν_1=1) reaction).

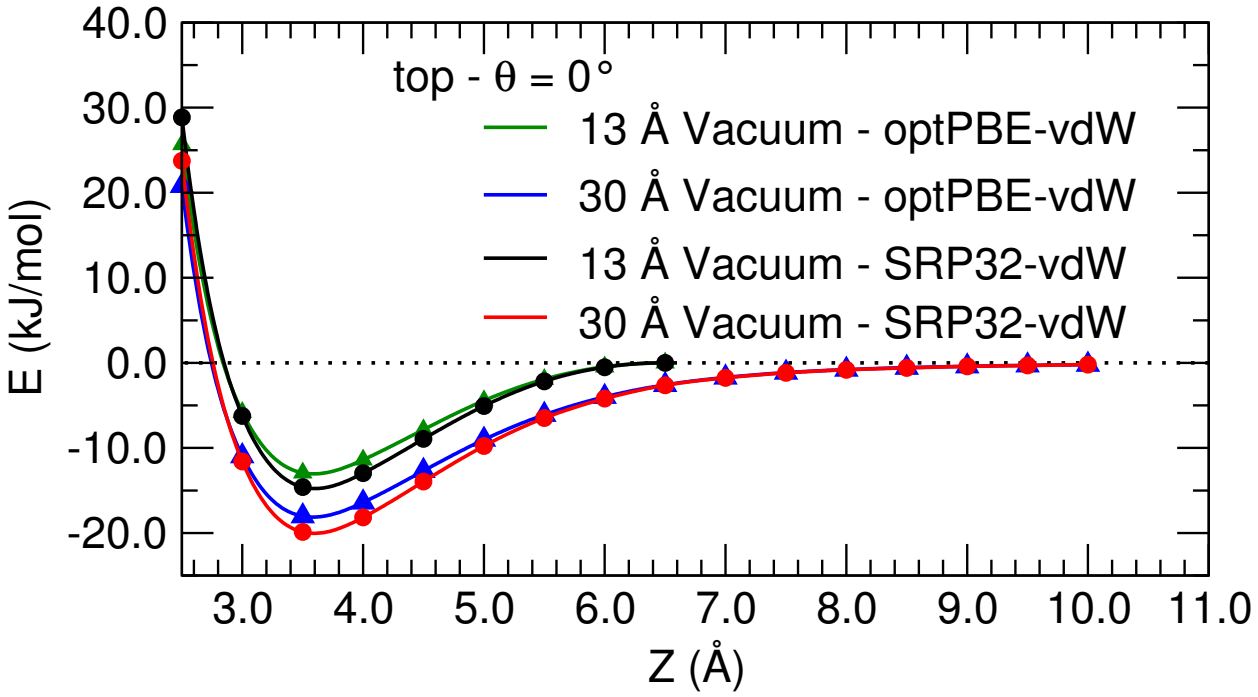

Figure S5. Interaction energy as a function of the distance between the center of mass of CH_4 and an ideal slab (Z), as computed with the SRP32-vdW functional and with the optPBE-vdW-DF functional of Ref.[74]. For the SRP32-vdW functional, the figure illustrates the energy profiles as calculated for two different computational setups differing only in the amount of vacuum space separating two slab's replicas, i.e., 13 and 30 Å, respectively.

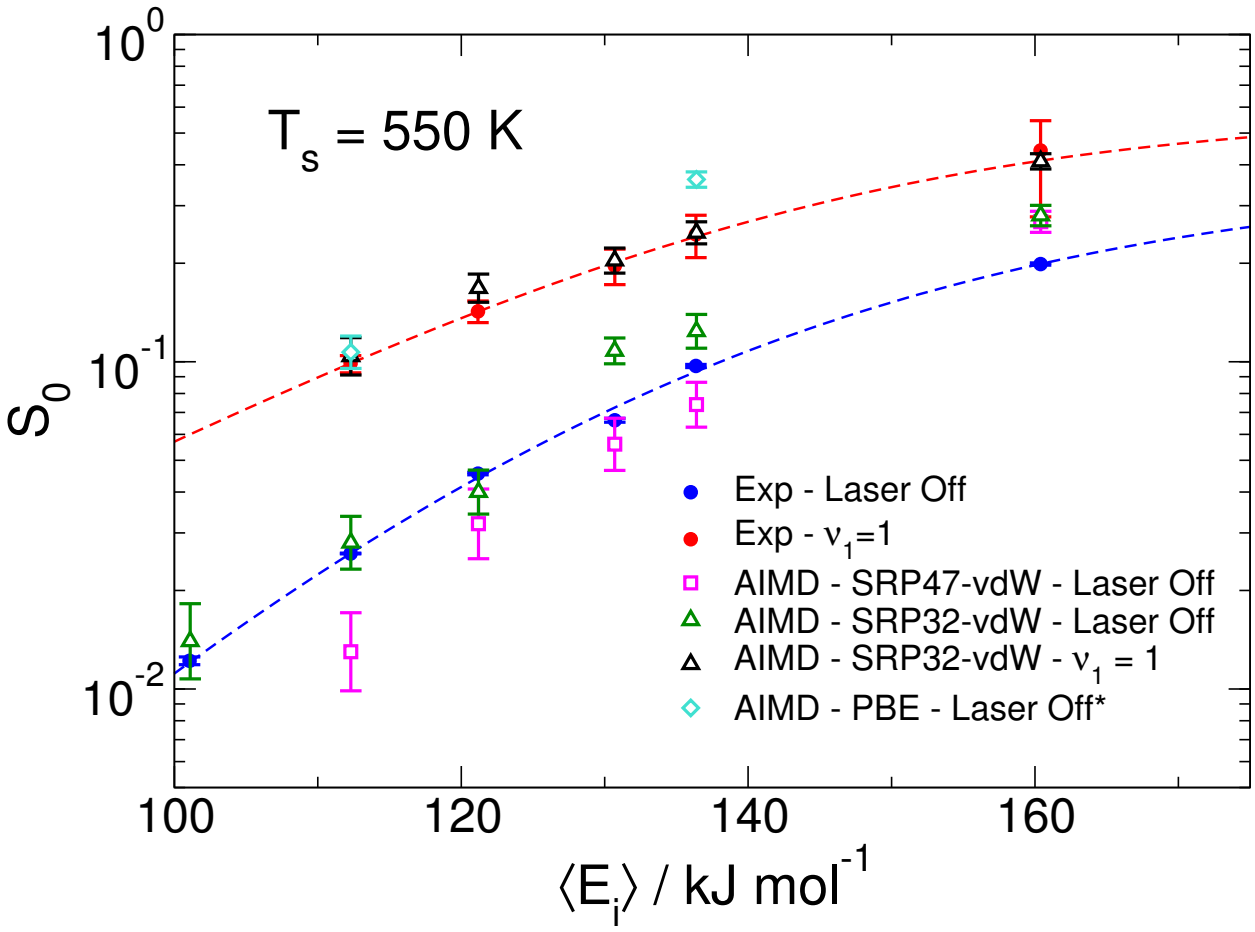

Figure S6. Reaction probabilities computed with AIMD are compared with experimental values. The red and blue dashed line represent fits of appropriate S-shaped curves to the experimental data for the two types of experiments addressed by theory: "Laser Off", in which the reactivity of a supersonic beam of molecules is measured, and "ν_1=1", in which the reactivity of CHD_3 pre-excited to the vibrational state in which the CH-stretch is excited with one quant is measured. Theoretical results are also presented for the ground vibrational state of CHD_3. Numbers present the horizontal distance (in kJ/mol) of the computed reaction probabilities to the fitted curves through the experimental data. Error bars in S_0 represent 68% confidence intervals. The state resolved experimental reaction probabilities were obtained from experiment and theory using method 1 (see Section 5), as in the main paper.

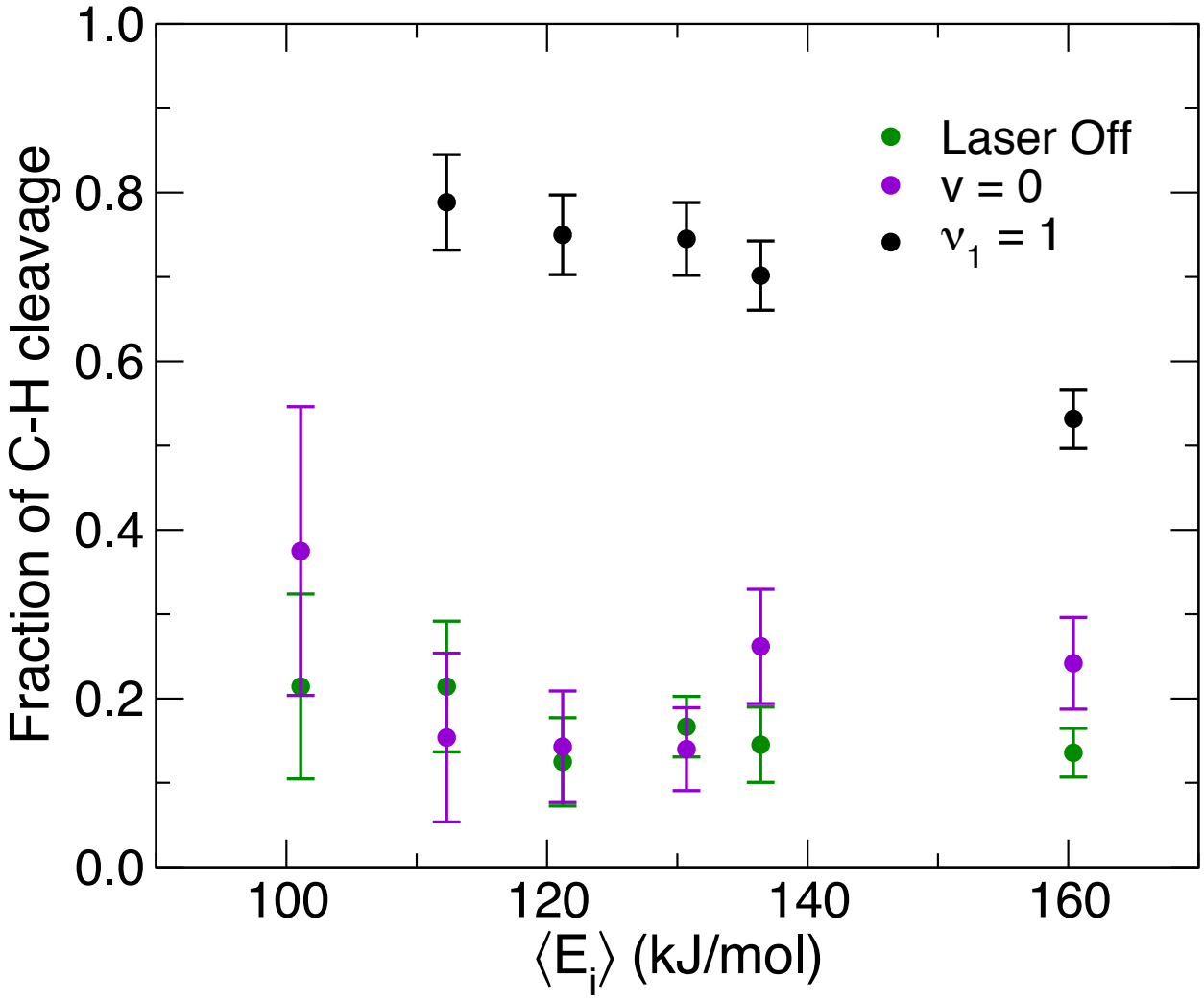

Figure S7. The fraction of CHD_3 molecules dissociating via C-H bond cleavage computed with AIMD is plotted as a function of the average incidence energy, for laser-off reaction (green symbols) and reaction of CHD_3 in its v=0 vibrational ground state (purple symbols) and in its ν_1 = 1 vibrationally excited state (black symbols).

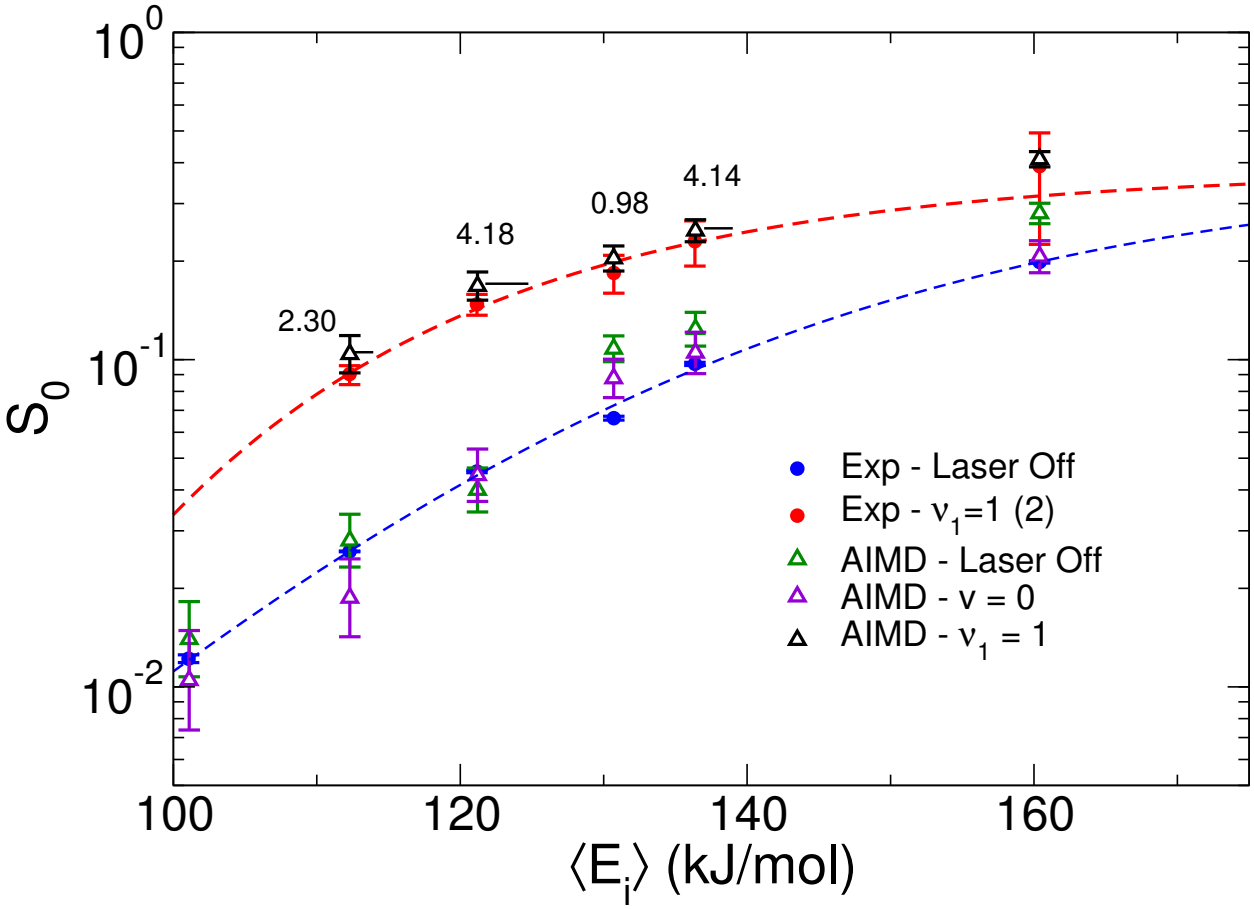

Figure S8. Reaction probabilities computed with AIMD are compared with experimental values. The red and blue dashed line represent fits of appropriate S-shaped curves to the experimental data for the two types of experiments addressed by theory: "Laser Off", in which the reactivity of a supersonic beam of molecules is measured, and "ν_1=1", in which the reactivity of CHD_3 pre-excited to the vibrational state in which the CH-stretch is excited with one quant is measured. Theoretical results are also presented for the ground vibrational state of CHD_3. Numbers present the horizontal distance (in kJ/mol) of the computed reaction probabilities to the fitted curves through the experimental data. Error bars in S_0 represent 68% confidence intervals. The state resolved experimental reaction probabilities were obtained from experiment and theory using method 2.

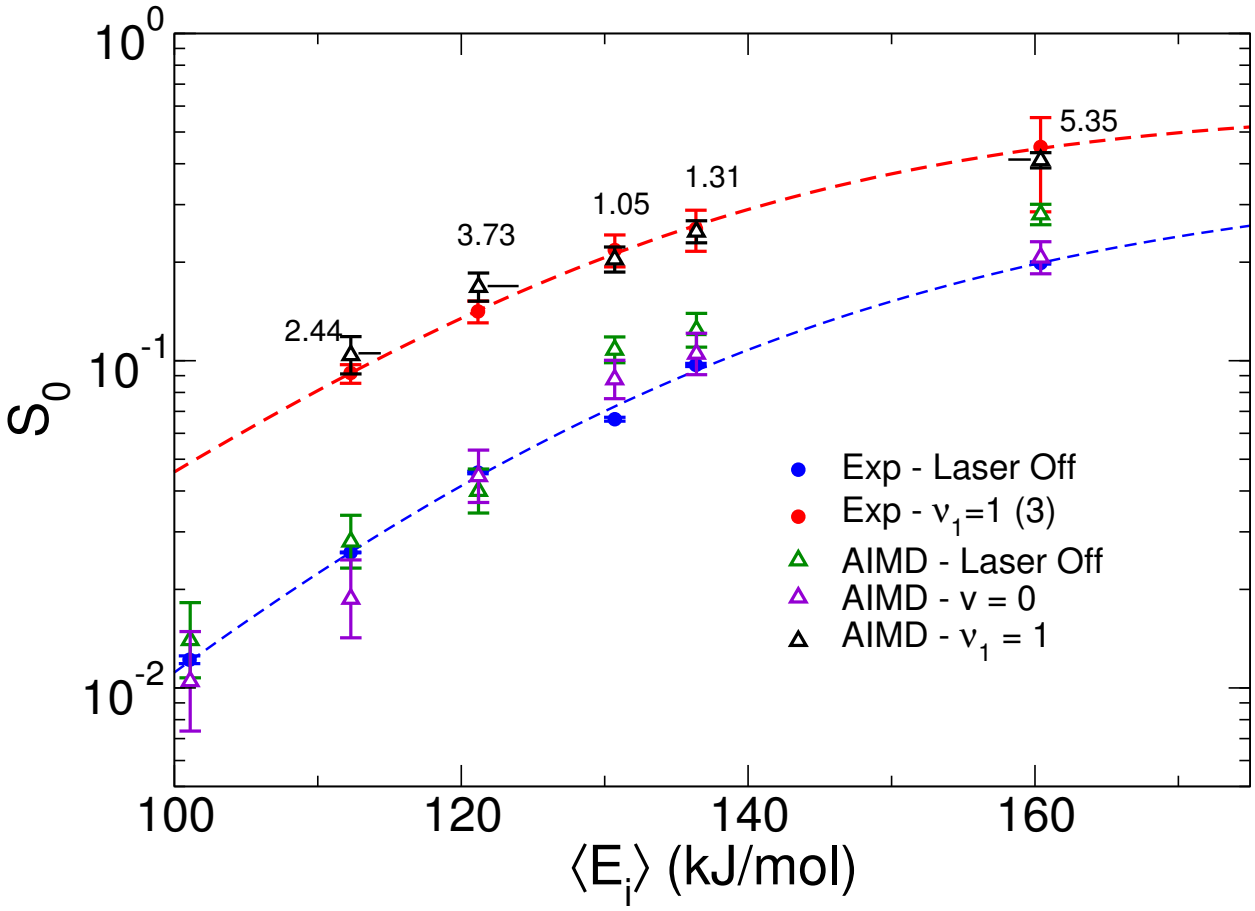

Figure S9. Reaction probabilities computed with AIMD are compared with experimental values. The red and blue dashed line represent fits of appropriate S-shaped curves to the experimental data for the two types of experiments addressed by theory: "Laser Off", in which the reactivity of a supersonic beam of molecules is measured, and "ν_1=1", in which the reactivity of CHD_3 pre-excited to the vibrational state in which the CH-stretch is excited with one quant is measured. Theoretical results are also presented for the ground vibrational state of CHD_3. Numbers present the horizontal distance (in kJ/mol) of the computed reaction probabilities to the fitted curves through the experimental data. Error bars in S_0 represent 68% confidence intervals. The state resolved experimental reaction probabilities were obtained from experiment and theory using method 3.

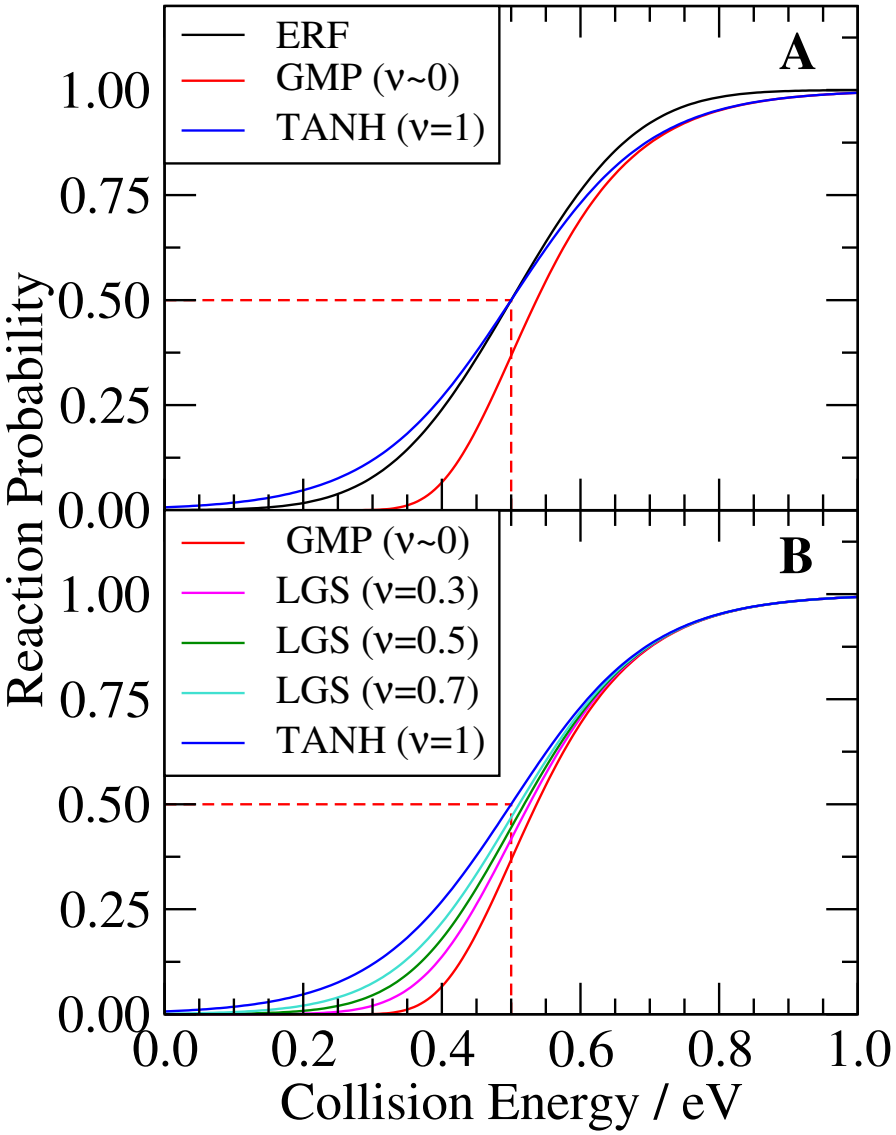

Figure S10. Illustrative representation of functions that can be used to represent idealized reaction probability curves, assuming a maximum value of the reaction probability A=1 The Gompertz (GMP) and hyperbolic tangent (TANH) are limiting values of the generalized logistics (LGS) function, with ν equal to 0 and 1, respectively. Also shown is a form based on the error function (ERF). All functions are plotted for a W value of 0.1 eV, and an E_0 value of 0.5 eV.

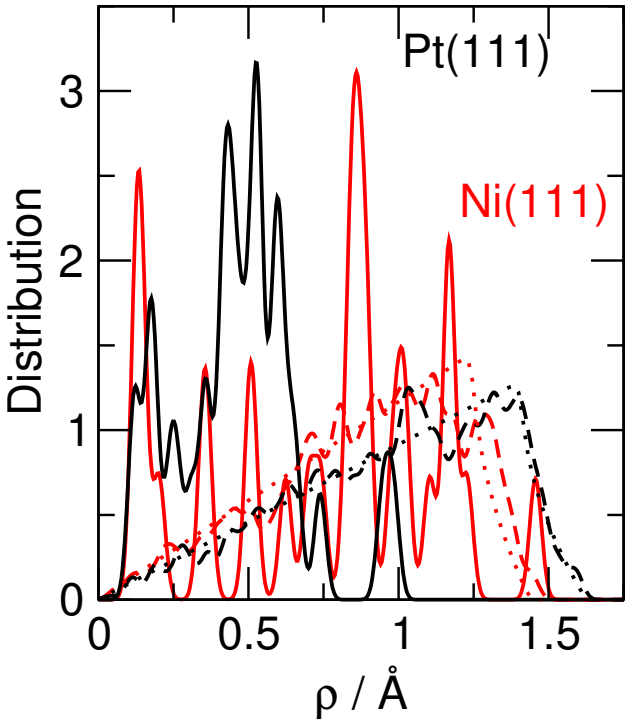

Figure S11. Impact parameters in collisions of CHD_3 with Ni(111) and Pt(111). (A) Probability distributions of the lateral distance ρ between CHD_3 and the nearest surface layer Ni (red) or Pt (black) atom. Dashed and solid lines show initial distributions of all incident molecules and those that react, respectively. The dotted line illustrates uniform sampling.

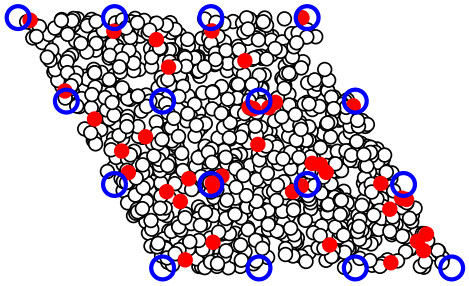

Laser Off - 121.2 kJ/mol

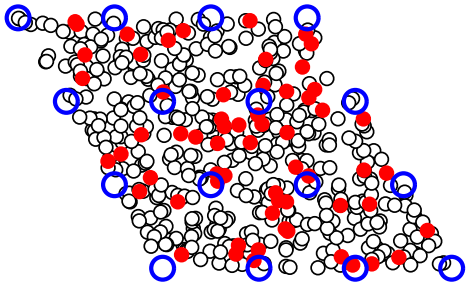

Laser Off - 136.4 kJ/mol

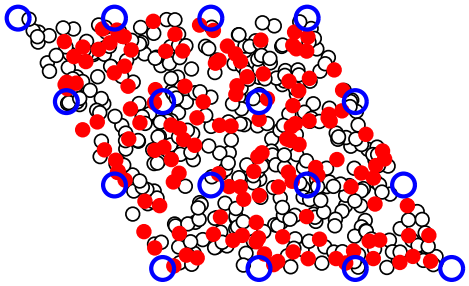

Laser Off - 160.4 kJ/mol

Figure S12. Initial distributions of impact sites for CHD_3 reacting on (red circles) and scattering from (white circles) Ni(111) are shown for laser-off conditions, and the three average incidence energies indicated. Blue circles indicate first layer atoms in ideal positions.

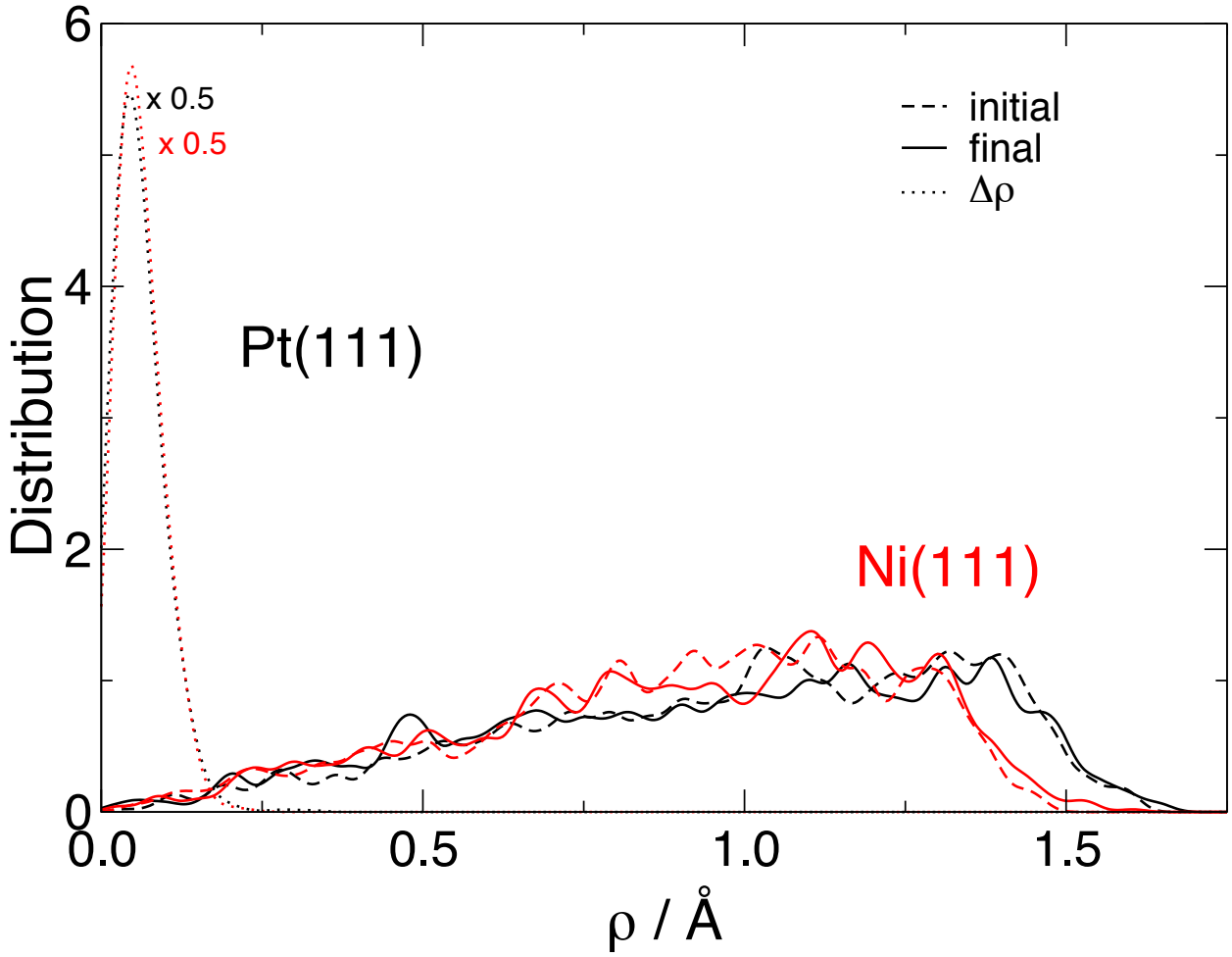

Figure S13. Distributions of impact parameters (the lateral distance ρ of CHD_3 to the nearest surface layer Pt or Ni atom) of CHD_3 reacting on and scattering from Ni(111) and Pt(111) under conditions where the reaction probability is approximately 0.03 in both systems (see main paper, Figure 3). The dotted lines indicate the lateral distance from the initial (*X*,*Y*) impact point to the final impact point, where "final" refers to the point where reaction occurs for reacting molecules and to the point of closest approach of the molecule to the surface for scattering molecules. The dashed lines indicate the distribution of the initial impact parameter, and the solid lines the impact parameter at either the point of reaction (for reaction) or at the distance of closest approach (for scattering).

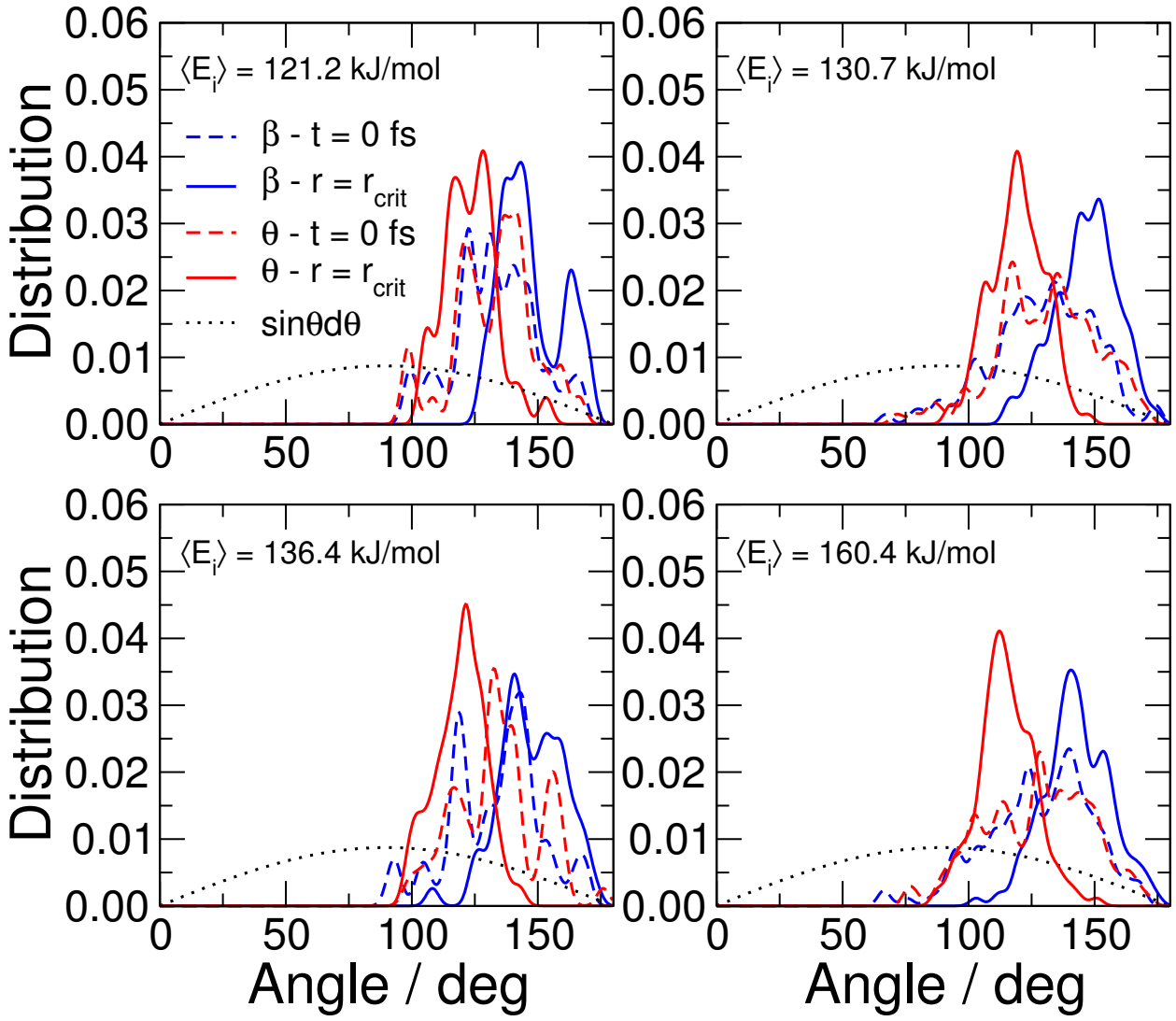

Figure S14. Molecular orientation in reactive collisions of CHD_3 with Ni(111). Probability distributions are shown for reactive collisions for E_i = 121.2, 130.7, 136.4, and 160.4 kJ/mol, for the angle the reactive CH bond, θ (red traces), and the principal axis of the methyl fragment, β (blue traces), makes with the surface normal (see Fig.2). Dashed and solid traces represent initial orientations and orientations at the point of reaction, respectively. The dotted lines illustrate random uniform sampling of these polar angles.

References.

(1) Juurlink, L. B. F.; Killelea, D. R.; Utz, A. L. State-resolved probes of methane dissociation dynamics. *Prog. Surf. Sci.* **2009,** *84*, 69-134.

(2) Smith, R. R.; Killelea, D. R.; DelSesto, D. F.; Utz, A. L. Preference for vibrational over translational energy in a gas-surface reaction. *Science* **2004,** *304*, 992-995.

(3) Killelea, D. R.; Campbell, V. L.; Shuman, N. S.; Utz, A. L. Bond-selective control of a heterogeneously catalyzed reaction. *Science* **2008,** *319*, 790-793.

(4) Beck, R. D.; Utz, A. L. Quantum-State Resolved Gas/Surface Reaction Dynamics Experiments. In *Dynamics of Gas-Surface Interactions: Atomic-Level Understanding of Scattering Processes at Surfaces*, Diéz Muiño, R.; Busnengo, H. F., Eds. Springer-Verlag: Berlin, 2013.

(5) Juurlink, L. B. F.; McCabe, P. R.; Smith, R. R.; DiCologero, C. L.; Utz, A. L. Eigenstate-Resolved Studies of Gas-Surface Reactivity: $CH_4(\nu_3)$ Dissociation on Ni(100). *Phys.Rev.Lett.* **1999,** *83*, 868-871.

(6) Juurlink, L. B. F.; Smith, R. R.; Utz, A. L. The role of rotational excitation in the activated dissociative chemisorption of vibrationally excited methane on Ni(100). *Faraday Discuss.* **2000,** *117*, 147-160.

(7) Juurlink, L. B. F.; Smith, R. R.; Utz, A. L. Controlling Surface Chemistry with Light: Spatially Resolved Deposition of Rovibrational-State-Selected Molecules. *J.Phys.Chem.B* **2000,** *104*, 3327-3336.

(8) McBabe, P. R.; Juurlink, L. B. F.; Utz, A. L. A molecular beam apparatus for eigenstate-resolved studies of gas-surface reactivity. *Rev.Sci.Instrum.* **2000,** *71*, 42-53.

(9) Auerbach, D. J. In *Atomic and Molecular Beam Methods*, Scoles, G., Ed. Oxford University Press: New York/Oxford, 1988; Vol. 1, pp 362-379.

(10) Michelsen, H. A.; Auerbach, D. J. A critical-examination of data on the dissociative adsorption and associative desorption of hydrogen at copper surfaces. *J. Chem. Phys.* **1991,** *94*, 7502-7520.

(11) Juurlink, L. B. F. Eigenstate-resolved measurements of methane dissociation on Ni(100). Ph.D. thesis, Tufts University, Medford, MA, 2000.

(12) Smith, R. R. Rovibrational-state-resolved studies of methane dissociation on Ni(111). Ph.D. thesis, Tufts University, Medford, MA, 2003.

(13) Bronnikov, D. K.; Kalinin, D. V.; Rusanov, V. D.; Filimonov, Y. G.; Selivanov, Y. G.; Hilico, J. C. Spectroscopy and Non-Equilibrium Distribution of Vibrationally Excited Methane in a Supersonic Jet. *J. Quant.Spectrosc.Radiat.Transfer* **1998,** *60*, 1053-1068.

(14) Yardley, J. T. *Introduction to molecular energy transfer*. Acedemic Press: New York, 1980.

(15) Killelea, D. R. Bond-Selective Control of a Gas-Surface Reaction. Ph.D. thesis, Tufts University, Medford, MA, 2007.

(16) Killelea, D. R.; Utz, A. L. On the origin of mode- and bond-selectivity in vibrationally mediated reactions on surfaces. *Phys.Chem.Chem.Phys*. **2013,** *15*, 20545.

(17) Hess, P.; Moore, C. B. Vibrational Energy Transfer in Methane and Methane-Rare-Gas Mixtures. *J.Chem.Phys*. **1976,** *65*, 2339.

(18) Miller, R. E. Infrared Laser Spectroscopy of molecular beams using a room temperature detector: Application to the study of translational freezing in free-jet expansions. *Rev. Sci. Instrum*. **1982,** *53*, 1719-1723.

(19) Faubel, M.; Schlemmer, S. A variable temperature bolometer for determining particle energy and absolute flux in molecular beams. *J. Phys. E: Sci. Instrum*. **1988,** *21*, 75-79.

(20) King, D. A.; Wells, M. G. Reaction mechanism in chemisorption kinetics. Nitrogen on the (100) plane of tungsten. *Proc.R.Soc.London Ser.A* **1974,** *339*, 245-269.

(21) Campbell, V. L. State Resolved Measurements of Surface Temperature Dependence and Isotopically Selective Reactivity of Methane on Ni(111). Ph.D. thesis, Tufts University, Medford, MA, 2011.

(22) Johnson, A. D.; Daley, S. P.; Utz, A. L.; Ceyer, S. T. The Chemistry of Bulk Hydrogen: Reaction of Hydrogen Embedded in Nickel with Adsorbed CH_3. *Science* **1992,** *257*, 223-225.

(23) Nattino, F.; Ueta, H.; Chadwick, H.; van Reijzen, M. E.; Beck, R. D.; Jackson, B.; van Hemert, M. C.; Kroes, G. J. Ab initio molecular dynamics calculations versus quantum-state-resolved experiments on CHD_3 + Pt(111): New insights into a prototypical gas-surface reaction. *J.Phys.Chem.Lett*. **2014,** *5*, 1294-1299.

(24) Groß, A.; Dianat, A. Hydrogen dissociation dynamics on precovered Pd surfaces: Langmuir is still right. *Phys.Rev.Lett.* **2007,** *98*, 206107.

(25) Nave, S.; Jackson, B. Methane dissociation on Ni(111): The role of lattice reconstruction. *Phys.Rev.Lett.* **2007,** *98*, 173003.

(26) Chuang, Y. Y.; Radhakrishnan, M. L.; Fast, P. L.; Cramer, C. J.; Truhlar, D. G. Direct dynamics for free radical kinetics in solution: Solvent effect on the rate constant for the reaction of methanol with atomic hydrogen. *J.Phys.Chem.A* **1999,** *103*, 4893-4909.

(27) Díaz, C.; Pijper, E.; Olsen, R. A.; Busnengo, H. F.; Auerbach, D. J.; Kroes, G. J. Chemically accurate simulation of a prototypical surface reaction: H_2 dissociation on Cu(111). *Science* **2009,** *326*, 832-834.

(28) Sementa, L.; Wijzenbroek, M.; van Kolck, B. J.; Somers, M. F.; Al-Halabi, A.; Busnengo, H. F.; Olsen, R. A.; Kroes, G. J.; Rutkowski, M.; Thewes, C., *et al*. Reactive scattering of H_2 from Cu(100): Comparison of dynamics calculations based on the specific reaction parameter approach to density functional theory with experiment. *J.Chem.Phys.* **2013,** *138*, 044708.

(29) Wang, X. G.; Sibert III, E. L. A nine-dimensional perturbative treatment of the vibrations of methane and its isotopomers. *J.Chem.Phys.* **1999,** *111*, 4510-4522.

(30) Czakó, G.; Bowman, J. M. Dynamics of the reaction of methane with chlorine atom on an accurate potential surface. *Science* **2011,** *334*, 343-346.

(31) Jiang, B.; Liu, R.; Li, J.; Xie, D. Q.; Yang, M. H.; Guo, H. Mode selectivity in methane dissociative chemisorption on Ni(111). *Chem. Sci.* **2013,** *4*, 3249-3254.

(32) Shen, X. J.; Chen, J.; Zhang, Z. J.; Shao, K. J.; Zhang, D. H. Methane dissociation on Ni(111): A fifteen-dimensional potential energy surface using neural network method. *J. Chem. Phys.* **2015,** *143*, 144701.

(33) Hundt, P. M.; Jiang, B.; van Reijzen, M. E.; Guo, H.; Beck, R. D. Vibrationally promoted dissociation of water on Ni(111). *Science* **2014,** *344*, 504-507.

(34) Nave, S.; Jackson, B. Vibrational mode-selective chemistry: Methane dissociation on Ni(100). *Phys.Rev.B* **2010,** *81*, 233408.

(35) Jackson, B.; Nave, S. The dissociative chemisorption of methane on Ni(111): The effects of molecular vibration and lattice motion. *J.Chem.Phys.* **2013,** *138*, 174705.

(36) Guo, H.; Jackson, B. Mode- and bond-selective chemistry on metal surfaces: The dissociative chemisorption of CHD_3 on Ni(111). *J.Phys.Chem.C* **2015,** *119*, 14769-14779.

(37) Farjamnia, A.; Jackson, B. The dissociative chemisorption of water on Ni(111): Mode- and bond-selective chemistry on metal surfaces. *J.Chem.Phys.* **2015,** *142*, 234705.

(38) Shen, X. J.; Lozano, A.; Dong, W.; Busnengo, H. F.; Yan, X. H. Towards bond selective chemistry from first principles: Methane on metal surfaces. *Phys.Rev.Lett.* **2014,** *112*, 046101.

(39) Lozano, A.; Shen, X. J.; Moiraghi, R.; Dong, W.; Busnengo, H. F. Cutting a chemical bond with demon's scissors: Mode- and bond-selective reactivity of methane on metal surfaces. *Surf.Sci.* **2015,** *640*, 25-35.

(40) Wijzenbroek, M.; Kroes, G. J. The effect of the exchange-correlation functional on H_2 dissociation on Ru(0001). *J.Chem.Phys.* **2014,** *140*, 084702.

(41) Wijzenbroek, M.; Klein, D. M.; Smits, B.; Somers, M. F.; Kroes, G. J. Performance of a non-local van der Waals density functional on the dissociation of H_2 on metal surfaces. *J.Phys.Chem.A* **2015,** *119*, 12146-12158.

(42) Liu, R.; Yang, M. H.; Czako, G.; Bowman, J. M.; Li, J.; Guo, H. Mode selectivity for a "central" barrier reaction: Eight-dimensional quantum studies of the $O(^3P) + CH_4 \rightarrow OH + CH_3$ reaction on an ab initio potential energy surface. *J.Phys.Chem.Lett.* **2012,** *3*, 3776-3780.

(43) Krupski, A. Debye temperature of the Pb layers on Ni(111). *Phys. Stat. Sol. (b)* **2006,** *243*, 467-472.

(44) Lyon, H. B.; Somorjai, G. A. Surface Debye Temperatures of the (100), (111), and (110) faces of platinum. *J.Chem.Phys.* **1966,** *44*, 3707-3711.

(45) Weinberg, W. H. Application of Debye-Waller theory to atomic and molecular scattering from solid surfaces. *J.Chem.Phys.* **1972,** *57*, 5463-5466.

(46) Takeuchi, W.; Yamamura, Y. Ne neutral atoms 180° backscattered from a Pt(111) surface in the three-atom scattering model. *Surf.Sci.* **1992,** *277*, 351-358.

(47) Nattino, F.; Migliorini, D.; Bonfanti, M.; Kroes, G. J. Methane dissociation on Pt(111): Searching for a specific reaction parameter density functional. *J.Chem.Phys.* **2016,** *144*, 044702.

(48) Gergen, B.; Nienhaus, H.; Weinberg, W. H.; McFarland, E. W. Chemically Induced Electronic Excitations at Metal Surfaces. *Science* **2001,** *294*, 2521-2523.

(49) Golibrzuch, K.; Bartels, N.; Auerbach, D. J.; Wodtke, A. M. The dynamics of molecular interactions and chemical reactions at metal surfaces: Testing the foundations of theory. *Annu.Rev.Phys.Chem.* **2015,** *66*, 399-425.

(50) Michaelson, H. B. The work function of the elements and its periodicity. *J.Appl.Phys.* **1977,** *48*, 4729-4733.

(51) Ramírez-Solís, A. On the accuracy of the complete basis set extrapolation for anionic systems: A case study of the electron affinity of methane. *Comput. Chem.* **2014,** *2*, 31-41.

(52) White, J. D.; Chen, J.; Matsiev, D.; Auerbach, D. J.; Wodtke, A. M. Conversion of Large-Amplitude Vibration to Electron Excitation at a Metal Surface. *Nature* **2005,** *433*, 503-505.

(53) Nieto, P.; Pijper, E.; Barredo, D.; Laurent, G.; Olsen, R. A.; Baerends, E. J.; Kroes, G. J.; Farías, D. Reactive and Non-reactive Scattering of H_2 from a Metal Surface is Electronically Adiabatic *Science* **2006,** *312*, 86-89.

(54) Cízek, M.; Horácek, J.; Domcke, W. Nuclear dynamics of the H_2^- collision complex beyond the local approximation: associative detachment and dissociative attachment to rotationally and vibrationally excited molecules. *J.Phys.B* **1998,** *31*, 2571-2583.

(55) Jiang, B.; Alducin, M.; Guo, H. Electron-hole pair effects in polyatomic dissociative chemisorption: Water on Ni(111). *J.Phys.Chem.Lett.* **2016,** *7*, 327-331.

(56) Jiang, B.; Guo, H. Dynamics of water dissociative chemisorption on Ni(111): Effects of impact sites and incident angles. *Phys.Rev.Lett.* **2015,** *114*, 166101.

(57) Blanco-Rey, M.; Juaristi, J. I.; Díez Muiño, R.; Busnengo, H. F.; Kroes, G. J.; Alducin, M. Electronic friction dominates hydrogen hot-atom relaxation on Pd(100). *Phys.Rev.Lett.* **2014,** *112*, 103203.

(58) Herzberg, G. *Molecular Spectra and Molecular Structure. Volume 2 - Infrared and Raman spectra of polyatomic molecules*. Krieger: Malabar, 1989.

(59) Askerka, M.; Maurer, R. J.; Batista, V. S.; Tully, J. C. Role of tensorial friction in energy transfer at metal surfaces. *Phys.Rev.Lett.* **2016,** *116*, 217601.

(60) Luntz, A. C.; Makkonen, I.; Persson, M.; Holloway, S.; Bird, D. M.; Mizielinski, M. S. Comment on "Role of Electron-Hole Pair Excitations in the Dissociative Adsorption of Diatomic Molecules on Metal Surfaces". *Phys.Rev.Lett.* **2009,** *102*, 109601.

(61) Chakraborty, A.; Zhao, Y.; Lin, H.; Truhlar, D. G. Combined valence bond-molecular mechanics potential-energy surface and direct dynamics study of rate constants and kinetic isotope effects for the $H+C_2H_6$ reaction. *J. Chem. Phys.* **2006,** *124*, 044315.

(62) Perdew, J. P.; Ruzsinszky, A.; Tao, J. M.; Staroverov, V. N.; Scuseria, G. E.; Csonka, G. I. Prescription for the design and selection of density functional approximations: More constraint satisfaction with fewer fits. *J.Chem.Phys.* **2005,** *123*, 062201.

(63) Peverati, R.; Truhlar, D. G. Quest for a universal density functional: the accuracy of density functionals accross a broad spectrum of databases in chemistry and physics. *Phil.Trans. R. Soc. A* **2014,** *372*, 20120476.

(64) Perdew, J. P.; Burke, K.; Ernzerhof, M. Generalized gradient approximation made simple. *Phys. Rev. Lett.* **1996,** *77*, 3865-3868.

(65) Hammer, B.; Hansen, L. B.; Nørskov, J. K. Improved adsorption energetics within density-functional theory using revised Perdew-Burke-Ernzerhof functionals. *Phys. Rev. B* **1999,** *59*, 7413-7421.

(66) Perdew, J. P.; Burke, K.; Ernzerhof, M. Erratum: Generalized gradient approximation made simple. *Phys. Rev. Lett.* **1997,** *78*, 1396-1396.

(67) Nattino, F.; Díaz, C.; Jackson, B.; Kroes, G. J. Effect of Surface Motion on the Rotational Quadrupole Alignment Parameter of D_2 Reacting on Cu(111). *Phys. Rev. Lett.* **2012,** *108*, 236104.

(68) Nieto, P.; Farías, D.; Miranda, R.; Luppi, M.; Baerends, E. J.; Somers, M. F.; van der Niet, M. J. T. C.; Olsen, R. A.; Kroes, G. J. Diffractive and reactive scattering of H_2 from Ru(0001): experimental and theoretical study. *Phys.Chem.Chem.Phys.* **2011,** *13*, 8583-8597.

(69) Groot, I. M. N.; Ueta, H.; van der Niet, M. J. T. C.; Kleyn, A. W.; Juurlink, L. B. F. Supersonic molecular beam studies of dissociative adsorption of H_2 on Ru(0001). *J. Chem. Phys.* **2007,** *127*, 244701.

(70) Perdew, J. P.; Chevary, J. A.; Vosko, S. H.; Jackson, K. A.; Pederson, M. R.; Singh, D. J.; Fiolhais, C. Atoms, molecules, solids, and surfaces: applications of the generalized gradient approximation for exchange and correlation. *Phys.Rev.B* **1992,** *46*, 6671-6687.

(71) Honkala, K.; Hellman, A.; Remediakis, I. N.; Logadottir, A.; Carlsson, A.; Dahl, S.; Cristensen, C. H.; Nørskov, J. K. Ammonia synthesis from first-principles calculations. *Science* **2005,** *307*, 555-558.

(72) Dion, M.; Rydberg, H.; Schröder, E.; Langreth, D. C.; Lundqvist, B. I. Van der Waals density functional for general geometries. *Phys. Rev. Lett.* **2004,** *92*, 246401.

(73) Berland, K.; Cooper, V. R.; Lee, K.; Schröder, E.; Thonhauser, T.; Hyldgaard, P.; Lundqvist, B. I. van der Waals forces in density functional theory: a review of the vdW-DF method. *Rep.Prog.Phys.* **2015,** *78*, 066501.

(74) Klimeš, J.; Bowler, D. R.; Michaelides, A. Chemical accuracy for the van der Waals density functional. *J.Phys.-Condens. Mater.* **2010,** *22*, 022201.

(75) London, F. Zur Theorie und Systematik der Molekularkräfte. *Z. Phys.* **1930,** *63*, 245-279.

(76) Berland, K.; Hyldgaard, P. Exchange functional that tests the robustness of the plasmon description of the van der Waals density functional. *Phys.Rev.B* **2014,** *89*, 035412.

(77) Berland, K.; Arter, C. A.; Cooper, V. R.; Lee, K.; Lundqvist, B. I.; Schröder, E.; Thonhauser, T.; Hyldgaard, P. van der Waals density functionals built upon the electron-gas tradition: Facing the challenge of competing interactions. *J.Chem.Phys.* **2014,** *140*, 18A539.

(78) Nave, S.; Tiwari, A. K.; Jackson, B. Dissociative chemisorption of methane on Ni and Pt surfaces: mode specific chemistry and the effects of lattice motion. *J.Phys.Chem.A* **2014,** *118*, 9615-9631.

(79) Zhang, Y.; Yang, W. Comment on "Generalized gradient approximation made simple". *Phys.Rev.Lett.* **1998,** *80*, 890-890.

(80) Klimeš, J.; Bowler, D. R.; Michaelides, A. Van der Waals density functionals applied to solids. *Phys.Rev.B* **2011,** *83*, 195131.

(81) Wellendorff, J.; Lundgaard, K. T.; Jacobsen, K. W.; Bligaard, T. mBEEF: An accurate semi-local Bayesian error estimation density functional. *J.Chem.Phys.* **2014,** *140*, 144107.

(82) Gautier, S.; Steinmann, S. N.; Michel, C.; Fleurat-Lessard, P.; Sautet, P. Molecular adsorption at Pt(111): How accurate are DFT functionals? *Phys.Chem.Chem.Phys.* **2015,** *17*, 28921-28930.

(83) Perdew, J. P.; Ruzsinszky, A.; Csonka, G. I.; Vydrov, O. A.; Scuseria, G. E.; Constantin, L. A.; Zhou, X. L.; Burke, K. Restoring the density gradient expansion for exchange in solids and surfaces. *Phys.Rev.Lett.* **2008,** *100*, 136406.

(84) Tkatchenko, A. Current understanding of van der Waals effects in realistic materials. *Adv.Funct.Mater.* **2015,** *25*, 2054-2061.

(85) Ruiz, V. G.; Liu, W.; Zojer, E.; Scheffler, M.; Tkatchenko, A. Density-functional theory with screened van der Waals interactions for the modeling of hybrid inorganic-organic systems. *Phys.Rev.Lett.* **2012,** *108*, 146103.

(86) Furche, F. Molecular tests of the random phase approximation to the exchange-correlation energy functional. *Phys.Rev.B* **2001,** *64*, 195120.

(87) Harl, J.; Kresse, G. Accurate bulk properties from approximate many body theories. *Phys.Rev.Lett.* **2009,** *103*, 056401.

(88) Tkatchenko, A.; Scheffler, M. Accurate molecular van der Waals interactions from ground-state electron density and free atom reference data. *Phys.Rev.Lett.* **2009,** *102*, 073005.

(89) Paier, J.; Marsman, M.; Hummer, K.; Kresse, G.; Gerber, I. C.; Ángyán, J. G. Screened hybrid density functionals applied to solids. *J.Chem.Phys.* **2006,** *124*, 154709.

(90) Stroppa, A.; Termentzidis, K.; Paier, J.; Kresse, G.; Hafner, J. CO adsorption on metal surfaces: A hybrid functional study with plane-wave basis set. *Phys. Rev. B* **2007,** *76*, 195440.

(91) Kroes, G. J.; Díaz, C. Quantum and classical dynamics of reactive scattering of H_2 from metal surfaces. *Chem.Soc.Rev.*, DOI:10.1039/c5cs00336a.

(92) Kresse, G.; Hafner, J. Ab-initio Molecular-Dynamics for Liquid-metals. *Phys. Rev. B* **1993,** *47*, 558-561.

(93) Kresse, G.; Hafner, J. Ab-Initio Molecular-Dynamics Simulation Of The Liquid-Metal Amorphous-Semiconductor Transition In Germanium. *Phys. Rev. B* **1994,** *49*, 14251-14269.

(94) Kresse, G.; Furthmüller, J. Efficiency of ab-initio total energy calculations for metals and semiconductors using a plane-wave basis set. *Comput. Mater. Sci.* **1996,** *6*, 15-50.

(95) Kresse, G.; Furthmüller, J. Efficient iterative schemes for ab initio total-energy calculations using a plane-wave basis set. *Phys. Rev. B* **1996,** *54*, 11169-11186.

(96) Kresse, G.; Joubert, D. From ultrasoft pseudopotentials to the projector augmented-wave method. *Phys. Rev. B* **1999,** *59*, 1758-1775.

(97) Blöchl, P. E. Projector Augmented-Wave Method. *Phys. Rev. B* **1994,** *50*, 17953-17979.

(98) Nave, S.; Tiwari, A. K.; Jackson, B. Methane dissociation and adsorption on Ni(111), Pt(111), Ni(100), Pt(100), and Pt(110)-(1×2): Energetic study. *J. Chem. Phys.* **2010,** *132*, 054705.

(99) Nave, S.; Jackson, B. Methane dissociation on Ni(111) and Pt(111): Energetic and dynamical studies. *J. Chem. Phys.* **2009,** *130*, 054701.

(100) Nave, S.; Jackson, B. Methane dissociation on Ni(111): The effects of lattice motion and relaxation on reactivity. *J.Chem.Phys.* **2007,** *127*, 224702.

(101) Prasanna, K. G.; Olsen, R. A.; Valdés, A.; Kroes, G. J. Towards an understanding of the vibrational mode specificity for dissociative chemisorption of CH_4 on Ni(111): A 15-dimensional study. *Phys.Chem.Chem.Phys.* **2010,** *12*, 7654-7661.

(102) Kresch, M.; Delaire, O.; Stevens, R.; Lin, J. Y. Y.; Fultz, B. Neutron scattering measurements of phonons in nickel at elevated temperatures. *Phys. Rev. B* **2007,** *75*, 104301.

(103) Henkelman, G.; Uberuaga, B. P.; Jónsson, H. A climbing image nudged elastic band method for finding saddle points and minimum energy paths. *J. Chem. Phys.* **2000,** *113*, 9901-9904.

(104) Henkelman, G.; Jónsson, H. Improved tangent estimate in the nudged elastic band method for finding minimum energy paths and saddle points. *J. Chem. Phys.* **2000,** *113*, 9978-9985.

(105) Manson, J. R. Energy transfer to phonons ai atom and molecule collisions with surfaces. In *Handbook of Surface Science*, Hasselbrink, E.; Lundqvist, B. I., Eds. Elsevier: 2008; Vol. 3.

(106) Manson, J. R. Inelastic scattering from surfaces. *Phys.Rev.B* **1991,** *43*, 6924-6937.

(107) Manson, J. R. Multiphonon atom-surface scattering. *Comput. Phys. Commun.* **1994,** *80*, 145-167.

(108)Simpson, W. R.; Rakitzis, T. P.; Kandel, S. A.; Orr-Ewing, A. J.; Zare, R. N. Reaction of Cl With Vibrationally Excited CH_4 and CHD_3 - State- to-State Differential Cross-Sections and Steric Effects For the HCl Product. *J.Chem.Phys*. **1995,** *103*, 7313-7335.

(109)Hase, W. L. *Encyclopedia of Computational Chemistry*. Wiley: New York, 1998.

(110)Liu, R.; Wang, F.; Jiang, B.; Czakó, G.; Yang, M.; Liu, K.; Guo, H. Rotational mode specificity in the $Cl + CHD_3 \rightarrow HCl + CD_3$ reaction. *J. Chem. Phys*. **2014,** *141*, 074310.

(111)Wilson, E. B. Probable Inference, the Law of Succession, and Statistical Inference. *J. Am. Statist. Assoc*. **1927,** *22*, 209-212.

(112)Díaz, C.; Olsen, R. A.; Auerbach, D. J.; Kroes, G. J. Six dimensional dynamics study of reactive and non reactive scattering of H_2 from Cu(111) using a chemically accurate potential energy surface. *Phys.Chem.Chem.Phys*. **2010,** *12*, 6499-6519.

(113)Herzberg, G. *Molecular Spectra and Molecular Structure. Volume 1 - Spectra of Diatomic Molecules*. Krieger: Malabar, 1989.

(114)Mastromatteo, M.; Jackson, B. The dissociative chemisorption of methane on Ni(100) and Ni(111): Classical and quantum studies based on the reaction path Hamiltonian. *J.Chem.Phys*. **2013,** *139*, 194701.

(115)Jiang, B.; Guo, H. Quantum and classical dynamics of water dissociation on Ni(111): A test of the site-averaging model in dissociative chemisorption oif polyatomic molecules. *J.Chem.Phys*. **2015,** *143*, 164705.

(116)Jiang, B.; Guo, H. Mode and bond selectivities in methane dissociative chemisorption: Quasi-classical trajectory studies on twelve-dimensional potential energy surface. *J.Phys.Chem.C* **2013,** *117*, 16127-16135.

(117)Zhang, D. H.; Light, J. C. Mode specificity in the H + HOD reaction. *J. Chem. Soc. Faraday Trans*. **1997,** *93*, 691-697.

(118)Czakó, G.; Liu, R.; Yang, M. H.; Bowman, J. M.; Guo, H. Quasiclassical trajectory studies of the $O(^3P) + CX_4(\nu_k = 0,1)$ -> $OX(\nu) + CX_3(n_1,n_2,n_3,n_4)$ reactions on an ab initio potential energy surface. *J.Phys.Chem.A* **2013,** *117*, 6409-6420.

(119)Zhang, Z.; Zhou, Y.; Zhang, D. H.; Czako, G.; Bowman, J. M. Theoretical study of the validity of the Polanyi rules for the late barrier Cl + CHD_3 reaction. *J.Phys.Chem.Lett.* **2012,** *3*, 3416-3419.

(120)Czako, G.; Bowman, J. M. Dynamics of the $O(^3P)$ + CHD_3 (v_{CH} = 0,1) reactions on an accurate ab initio potential energy surface. *Proc. Natl. Acad. Sci. U.S.A* **2012,** *109*, 7997-8001.

(121)Yan, S.; Wu, Y. T.; Zhang, B. L.; Yue, X. F.; Liu, K. Do vibrational excitations of CHD_3 preferentially promote reactivity toward the chlorine atom? *Science* **2007,** *316*, 1723-1726.

(122)Zhang, W. Q.; Kawamata, H.; Liu, K. CH stretching excitation in the early barrier F + CHD_3 reaction inhibits CH bond cleavage. *Science* **2009,** *325*, 303-306.

(123)Wang, F. Y.; Liu, K. Enlarging the reactive cone of acceptance by exciting the C-H bond in the $O(^3P)$ + CHD_3 reaction. *Chem.Sci.* **2010,** *1*, 126-133.

(124)Wang, F. Y.; Lin, J. S.; Chen, Y.; Liu, K. Vibrational enhancment factor of the Cl + $CHD_3(v_1=1)$ reaction: rotational-probe effects. *J.Phys.Chem.Lett.* **2013,** *4*, 323-327.

(125)Palma, J.; Clary, D. C. A quantum model Hamiltonian to treat reactions of the type X + YCZ_3 -> XY + CZ_3: Application to $O(^3P)$ + CH_4 -> OH + CH_3. *J.Chem.Phys.* **2000,** *112*, 1859-1867.

(126)Liu, R.; Xiong, H. W.; Yang, M. H. An eight-dimensional quantum mechanical Hamiltonian for X + YCZ_3 system and its applications to H + CH_4 reaction. *J.Phys.Chem.Lett.* **2012,** *3*, 3776-3780.

(127)Schiffel, G.; Manthe, U. Quantum dynamics of the H + CH_4 -> H_2 + CH_3 reaction in curvilinear coordinates: Full-dimensional and reduced dimensional calculations of reaction rates. *J.Chem.Phys.* **2010,** *132*, 084103.

(128)Stouffer, S. A.; Suchman, E. A.; DeVinney, L. C.; Star, S. A.; Williams, R. M., Jr. *Studies in Social Psychology in World War II. Vol.1: The American Soldier: Adjustment During Army Life* Princeton University Press: Princeton, 1949.

(129)Hays, W. L. *Statistics*. Holt--Saunders: Tokyo, 1981.

(130)Beckerle, J. D. Ph.D. thesis. Massachusetts Institute of Technology, 1988.

(131)Beckerle, J. D.; Johnson, A. D.; Yang, Q. Y.; Ceyer, S. T. Collision induced dissociative chemisorption of CH_4 on Ni(111) by inert gas atoms: The mechanism for chemistry with a hammer. *J. Chem. Phys.* **1989,** *91*, 5756-5777.

(132)Nattino, F.; Genova, A.; Guijt, M.; Muzas, A. S.; Díaz, C.; Auerbach, D. J.; Kroes, G. J. Dissociation and recombination of D_2 on Cu(111): Ab initio molecular dynamics calculations and improved analysis of desorption experiments. *J.Chem.Phys.* **2014,** *141*, 124705.

(133)Campbell, V. L.; Chen, N.; Guo, H.; Jackson, B.; Utz, A. L. Substrate vibrations as promoters of chemical reactivity on metal surfaces. *J.Phys.Chem.A* **2015,** *119*, 12434-12441.

(134)Nattino, F. Ab Initio Molecular Dynamics calculations on reactions of molecules with metal surfaces. Ph.D. thesis, Leiden University, 2015.

(135)Gundersen, K.; Jacobsen, K. W.; Nørskov, J. K.; Hammer, B. The energetics and dynamics of H_2 dissociation on Al(110). *Surf.Sci.* **1994,** *304*, 131.

(136)Salin, A. Theoretical study of hydrogen dissociative adsorption on the Cu(110) surface. *J.Chem.Phys.* **2006,** *124*, 104704.

(137)Kroes, G. J. Towards a database of chemically accurate barrier heights for reactions of molecules with metal surfaces. *J.Phys.Chem.Lett.* **2015,** *6*, 4106-4114.

(138)Polanyi, J. C. Some concepts in reaction dynamics. *Science* **1987,** *236*, 680-690.

(139)Füchsel, G.; Thomas, P. S.; den Uyl, J.; Öztürk, Y.; Nattino, F.; Meyer, H.-D.; Kroes, G. J. Rotational effects on the dissociation dynamics of CHD_3 on Pt(111). *Phys.Chem.Chem.Phys.* **2016,** *13*, 8659-8670.

(140)Jackson, B.; Nave, S. The dissociative chemisorption of methane on Ni(100): Reaction path description of mode-selective chemistry. *J.Chem.Phys.* **2011,** *135*, 114701.

(141)Zheng, J. J.; Zhao, Y.; Truhlar, D. G. The DBH24/08 database and its use to assess electronic structure model chemistries for chemical reaction barrier heights. *J.Chem.Theory Comp.* **2009,** *5*, 808-821.

(142)Yang, K.; Zheng, J. J.; Zhao, Y.; Truhlar, D. G. Tests of the RPBE, revPBE, τ - HCTHhyb, ωB97X-D , and MOHLYP density functional approximations and 29 others against representative databases for diverse bond energies and barrier heights in catalysis. *J.Chem.Phys.* **2010,** *132*, 164117.

(143)Wellendorff, J.; Lundgaard, K. T.; Møgelhøj, A.; Petzold, V.; Landis, D. D.; Nørskov, J. K.; Bligaard, T.; Jacobsen, K. W. Density functionals for surface science: Exchange-correlation model development with Bayesian error estimation. *Phys.Rev.B* **2012,** *85*, 235149.

(144)Cohen, A. J.; Mori-Sánchez, P.; Yang, W. T. Insights into current limitations of density functional theory. *Science* **2008,** *321*, 792-794.

(145)Zhang, Y. K.; Yang, W. T. A challenge for density functionals: Self-interaction error increases for systems with a noninteger number of electrons. *J.Chem.Phys.* **1998,** *109*, 2604-2608.

(146)Cohen, A. J.; Mori-Sánchez, P.; Yang, W. T. Challenges for density functional theory. *Chem.Rev.* **2012,** *112*, 289-320.

(147)Perdew, J. P.; Parr, R. G.; Levy, M.; Balduz, J., J.L. Density-functional theory for fractional particle number: Derivative discontinuities of the energy. *Phys.Rev.Lett.* **1982,** *49*, 1691-1694.

(148)Janesko, B. G.; Barone, V.; Brothers, E. N. Accurate surface chemistry beyond the generalized gradient approximation: illustrations for graphene adatoms. *J. Chem. Theory Comput.* **2013,** *9*, 4853-4859.

(149)Janesko, B. G. Density functional theory beyond the generalized gradient approximation for surface chemistry. *Top. Cur. Chem.* **2015,** *365*, 25-52.

(150)Behler, J.; Delley, B.; Lorenz, S.; Reuter, K.; Scheffler, M. Dissociation of O_2 at Al(111): The role of spin selection rules. *Phys.Rev.Lett.* **2005,** *94*, 036104.

(151)Behler, J.; Reuter, K.; Scheffler, M. Nonadiabatic effects in the dissociation of oxygen molecules at the Al(111) surface. *Phys.Rev.B* **2008,** *77*, 115421.

(152)Pozzo, M.; Alfè, D. Hydrogen dissociation on Mg(0001) studied via quantum Monte Carlo calculations. *Phys.Rev.B* **2008,** *78*, 245313.

(153)Libisch, F.; Huang, C.; Liao, P. L.; Pavone, M.; Carter, E. A. Origin of the energy barrier to chemical reactions of O_2 on Al(111): Evidence for charge transfer, not spin selection. *Phys.Rev.Lett.* **2012,** *109*, 198303.

(154)Mosch, C.; Koukounas, C.; Bacalis, N.; Metropoulos, A.; Gross, A.; Mavridis, A. Interaction of dioxygen with Al clusters and Al(111): A comparative theoretical study. *J.Phys.Chem.C* **2008,** *112*, 6924-6932.

(155)Liu, H. R.; Xiang, H. J.; Gong, X. G. First principles study of adsorption of O_2 on Al surface with hybrid functionals. *J. Chem. Phys.* **2011,** *135*, 214702.

(156)Yuan, Q. H.; Li, J. B.; Fan, X. L.; Lau, W. M.; Liu, Z. F. A barrier for the Al_{13}^- + O_2 reaction and its implication for the chemisorption of O_2 on Al(111). *Chem.Phys.Lett.* **2010,** *489*, 16-19.

(157)Hayden, B. E.; Schweizer, E.; Kötz, R.; Bradshaw, A. M. The early stages of oxidation of magnesium single crystal surfaces. *Surf.Sci.* **1981,** *111*, 26-38.